Investigation of a prototype industrial gas turbine combustor using alternative gaseous fuels

Sigfrid, Ivan

2013

INVESTIGATION OF A PROTOTYPE INDUSTRIAL GAS TURBINE COMBUSTOR USING ALTERNATIVE GASEOUS FUELS

Doctoral Thesis

Ivan Sigfrid

Division of Thermal Power Engineering
Department of Energy Sciences

Lund, Sweden, 2013

LUND
UNIVERSITY

Thesis for the degree of Doctor of Philosophy in Engineering.
ISBN 978-91-7473-607-6 (print)
ISBN 978-91-7473-608-3 (pdf)
ISSN 0282-1990
ISRN LUTMDN/TMHP-13/1096-SE

Department of Energy Sciences, Division of Thermal Power Engineering
Faculty of Engineering
Lund University
Box 118
SE-221 00 LUND
Sweden

Cover photo by courtesy of Siemens Industrial Turbomachinery [SIT].
Typeset in LaTeX
Printed by Tryckeriet i E-huset, Lund 2013.

Populärvetenskaplig Sammanfattning

Jordens totala energiförbrukning stiger. Samtidigt förbrukas primärt fossila naturresurser som kan anses ändliga, så som olja, kol eller naturgas, för att tillgodose energibehovet. Även andra energikällor används, t.ex. kärnbränsle, vind och vatten. Denna avhandling fokuserar på energi som omvandlas vid förbränning av gas i gasturbiner. Eftersom naturgas är ett fossilt bränsle riktas forskning åt nyttjandet av alternativa gaser, vilket är tänkt minimera nettoproduktionen av koldioxid. Sådana alternativa gaser kan exempelvis vara förgasningsgas från kol där koldioxiden separerats innan förbränning eller biogas vars konsumtion och produktion av koldioxid tar ut vartannat. De mest grundläggande förutsättningarna för att sådana gaser ska kunna användas kommersiellt är att de ska kunna förbrännas kontrollerat, utan avbrott och utan att bidra till att farliga avgaser så som kväveoxider (NO_X), kolmonoxid eller oförbrända kolväten kommer ut i naturen. För att nå kommersiell framgång fordras även att den för stunden ekonomiskt sett mest fördelaktiga gasen kan användas. För att kunna nyttja olika gaser fordras en bränsleflexibel brännare vars befintliga brännkammare kan anpassas eller enkelt bytas ut beroende bränslets egenskaper. Denna avhandling redogör för undersökningen av hur en prototyp av en nydesignad brännkammare kan hantera alternativa gaser. De gaser som undersökts är syntetiska gaser så som förgasningsgaser med högt vätgasinnehåll och metanbaserade gaser med lågt energiinnehåll, vilka imiterar biogas. De ekonomiska aspekterna ligger utanför avhandlingens omfattning.

För att undersöka hur alternativa gaser beter sig vid förbränning undersöktes först deras flamhastighet i en simpel brännare av Bunsen typ. En sådan undersökning visar hur pass reaktiv en gas är, vilket kan användas till att förutse om en flamma vid förbränning av gasen kommer att stabiliseras i det tilltänkta förbränningsområdet eller om flamman riskerar att placera sig upp- eller nedströms. Att erhålla sådan information är av vikt eftersom felaktig placering av flamman kan leda till ostabil förbränning eller orsaka skador på brännkammaren. Därefter undersöktes själva brännaren vid både atmosfäriskt och högre tryck. Undersökningarna omfattade lokalisering av stabilitetsgränser, minimering av emissioner, visualisering av själva flamman och mätning av strömnings-

fält. Stabilitetsgränserna och emissionerna undersöktes genom tillförsel av olika mängder luft och bränsle i brännarens enskilda delar. Flammans positionering diagnosticerades med hjälp av laser som skapar ett fluorescerande ljus från molekyler som enbart fanns i flamman. För att mäta strömningsfältet tillsattes partiklar till förbränningsluften. Genom att använda laserljus och ett kamerasystem kunde sedan partiklarnas rörelse dokumenteras. De två laserteknikerna gav möjligheten att visualisera flammas placering och strömningsmönster. Ett ytterligare mål med de lasermätningar som genomfördes var att skapa mätresultat som kan nyttjas för validering av såkallade CFD-beräkningar, avancerade datorbaserade beräkningsmodeller för flöden.

Abstract

In this thesis, the effect of alternative gaseous fuels, with high hydrogen content and lower calorific value, on gas turbine combustion was investigated experimentally. The aim of the investigation was to find operational limitations for an experimental burner and to supply data for validation of computational fluid dynamics (CFD). Before examination of the actual burner, the laminar flame speed was measured for a range of gases. The measurement technique was based on Schlieren imaging which is a measure of the density gradient through a flame surface. A Bunsen type burner was used to measure the angle of a conical flame from which the laminar flame speed was calculated. In order to improve the comparability of these measurements with other measurement methods the laminar flame speed was corrected for the influence of stretch. The effect of stretch will increase or decrease the flame speed depending on the curvature of the flame and the physical properties of the gases involved in the combustion, e.g. the Lewis number and preferential diffusivity.

The gas turbine burner examined was a downscaled version of the burner that is now found in the commercial gas turbine, SGT-750. The burner consists of three concentric sections. The central part is a precombustor called rich-pilot-lean (RPL). The purpose of the RPL is to supply heat and radicals to the other sections to stabilize combustion. The next section is the Pilot, which serves as an intermediate burner in which the equivalence ratio can be optimized to stabilize combustion and minimize NO_X emissions. The outermost section is the Main. For the experimental burner approximately 79 % of the mass flow passes through this section. All sections have their own swirlers that create recirculation zones for flame stabilization. The experimental work in this thesis includes measurements of the lean stability limit, emission optimization (primarily NO_X), flame diagnostic through OH-Laser induced fluorescence (LIF) and particle image velocimetry (PIV). Tests were conducted at both atmospheric conditions with preheated air (650 K) and at elevated pressure up to 9 bar. Results from the experimental investigations were also used to validate CFD computations using reduced chemical kinetic schemes, and to validate reactor network calculations based on perfectly stirred reactors (PSR) and plug flow reactors (PFR).

Lean stability limit experiments showed how the RPL equivalence ratio could be optimized to lower the lean blowout limit. Increasing the RPL equivalence ratio was shown to extend the lean blowout limit, up to a limit after which the RPL flame was quenched. Reactor network modelling showed that the stabilizing effect of the RPL was a combination of thermal energy and reactive radicals supplied to the flame zone. The important radicals were shown to be H, O and OH.

The emission optimization measurements showed that lowering the equivalence ratio in both the RPL and the pilot minimized the NO_X emissions. CFD simulation showed that the degree of mixing of both the RPL and the Pilot at point of ignition was not perfect. Imperfect mixing causes pockets of stoichiometric mixtures to react, which in turn create hot spots where thermal NO_X can be formed. At rich RPL equivalence ratios, a flame could be visualized with OH-LIF after the RPL exit. This flame probably to some extent combusts closer to stoichiometry, which increases thermal NO_X. These theories of how NO_X is formed were confirmed by reactor network calculations.

Acknowledgements

Without inspiring social surroundings, i.e. family, friends and work companions, working on this thesis would have been tougher. Consequently, I would like to express my gratitude to the people who have made my work on this thesis easier.

Firstly, I would like to thank my wife Lisa and my sons Frode and Erik for their support and encouragement. I would like to thank my mother, Gunvor, for all her support. I would like to thank my sisters, Nanna, Malin, Sandra and their respective families.

I would like to thank my co-workers at the Division of Thermal Engineering. Jens Klingmann, my supervisor, has given me guidance throughout my work. Magnus Genrup has introduced me to the wonderful world of gas turbines. Marcus Thern has helped me on countless occasions to solve all sorts of editorial issues. I would also like to give gratitude to my fellow doctoral students (some of whom have already achieved their PhD) Pontus Eriksson, Magnus Fast, Klas Jonshagen, Björn Nyberg, Parisa Sayad, Majed Sammak, Srikanth Deshpande, Atanu Kundu, Mao Li and Saeed Bahrami. I would like to thank, our Post-doctoral researcher Alessandro Schönborn for helping me both on the football field and the scientific field. I would also like to thank our Post-doctoral researcher Maria Mondejar.

To avoid making the acknowledgements too long, I would like to thank all staff at the Department of Energy Sciences and the Division of Combustion Physics at the Department of Physics. However, I would like to thank a few in particular. Ronald Whiddon has been my laboratory partner during my PhD work, and I am very grateful for the numerous tasks he has performed. He was always happy to help even when times were tough. Rutger Lorensson was not only the main person responsible for making the pressurized testing possible; he is also the man who, magically, always has a solution to any technical difficulty that may arise. Thanks to Robert Collin and Andreas Lantz for stepping in to support the DESS rig work.

Abdallah "Abbe" Abou-Taouk, at Chalmers University of Technology, should be thanked for supplying CFD data to the project when needed.

This research has been funded by the Swedish Energy Agency, Siemens

Industrial Turbomachinery AB, GKN Aerospace Engine Systems Sweden AB, and the Royal Institute of Technology through the Swedish research program TURBO POWER, the support of which is gratefully acknowledged.

List of Papers

In this thesis 9 papers are appended. They are referred to in the text by their Roman numerals. The papers are appended at the end of the thesis in the following order.

I **Sigfrid, I. R.**, Whiddon, R., Collin, R., and Klingmann, J., 2013, "Reactive species influence on the lean blowout limit for an industrial DLE gas turbine burner", *Combustion and Flame, Submitted.*

II **Sigfrid, I. R.**, Whiddon, R., Collin, R., and Klingmann, J., 2013, "Experimental and Reactor Network Study of Nitrogen Dilution Effects on NO_X Formation for Natural Gas and Syngas at Elevated Pressures", *ASME Turbo Expo Conference Proceedings.*

III Whiddon, R., **Sigfrid, I. R.**, Collin, R., and Klingmann, J., 2013, "Investigation of a Premixed Gas Turbine Combustor Central Body Burner using OH Planar Laser Induced Fluorescence at Elevated Pressures", *ASME Turbo Expo Conference Proceedings.*

IV **Sigfrid, I. R.**, Whiddon, R., Abou-Taouk, A., Collin, R., and Klingmann, J., 2012, "Experimental Investigations of an Industrial Lean Premixed Gas Turbine Combustor with High Swirling Flow", *ASME Gas Turbine India Conference Proceedings.*

V Abou-Taouk, A., **Sigfrid, I. R.**, Whiddon, R., and Eriksson, L. E., 2012, "A Four-Step Global Reaction Mechanism for CFD Simulations of Flexi-Fuel Burner for Gas Turbines", *Turbulence, Heat and Mass Transfer 7, Palermo, Sicily, Italy.*

VI Abou-Taouk, A., Eriksson, L. E., **Sigfrid, I. R.**, and Whiddon, R., 2011, "CFD Investigation of Swirl-Stabilized Flexi-Fuel Burner Using Methane-Air Mixtures for Gas Turbines", *International Society for Air-Breathing Engines, ISABE.*

VII **Sigfrid, I. R.**, Whiddon, R., Aldén, M., and Klingmann, J., 2011, "Parametric Study of Emissions from Low Calorific Value Syngas Combustion, with Variation of Fuel Distribution, in a Prototype Three Sector Burner", *ASME Turbo Expo Conference Proceedings.*

VIII **Sigfrid, I. R.**, Whiddon, R., Aldén, M., and Klingmann, J., 2011, "Experimental Investigation of Lean Stability Limit of an Prototype Syngas Burner for Low Calorific Value Gases", *ASME Turbo Expo Conference Proceedings.*

IX **Sigfrid, I. R.**, Whiddon, R., Collin, R., and Klingmann, J., 2010, "Experimental Investigation of Laminar Flame Speeds for Medium Caloricic Gas with Various Amounts of Hydrogen and Carbon Monoxide content at Gas Turbine Temperatures", *ASME Turbo Expo Conference Proceedings.*

Other publications by the author

Genrup, M., **Carlsson, I.**, Engdar, U., and Assadi, M., 2005, "A Reduced-Order Through-Flow Program for Choked and Cooled Axial Turbines", *ASME Turbo Expo Conference Proceedings.*

NOMENCLATURE

A	pre exponential factor [$m^3/(K^b\,kmol\,s)$]
A_f	flame area [m^2]
A_{ref}	combustor reference area [m^2]
$A^2\Sigma^+$	first electronically excited state in the OH radical
a	empirical exponent
b	temperature exponent
CL	combustor loading [$kg/(s\,atm^{1.8}m^3)$]
c_p	specific heat at constant pressure [$J/(kg\,K)$]
Da	Damköhler number
Dil.	Diluted
D_L	diffusivity of limiting reactant [m^2/s]
D_{ref}	combustor reference diameter [m]
d_p	particle diameter [m]
dt	change in time [s]
E_a	activation energy [J/kmol]
f_{mp}	frequency of the modal pair [1/s]
H	lower specific heat energy of the fuel [J/kg]
H_F	heat available in the fuel [J/s]
I_0	stretch factor
Ka	Karlovitz number
k	rate coefficient [$m^3/(kmol\,s)$]
k_{1f}	rate coefficient [$m^3/(kmol\,s)$]
L	length [m]
Le	Lewis number
l_0	integral length scale [m]
l_c	chemical length scale [m]
$M_{rec.}$	recirculated mass flow [kg/s]
M_{tot}	total mass flow [kg/s]
m	pressure exponent
$\dot{m}$	mass flow [kg/s]
m_p	modal pair
n_v	number of vortices
n	reaction order
P	pressure [bar]

Q_{in}	heat input [J]
$Q_1(8)$	excitation transition of the OH radical
q	fuel/air ratio by mass
R	characteristic radius [m]
Re	Reynolds number
Re_{0b}	post combustion Reynolds number
Rec.	recirculated mass flow
R_u	universal gas constant [J/(K mol)]
r	radius [m]
r_i	inner radius [m]
r_o	outer radius [m]
S	specific entropy [J/(kg K)]
S_L	laminar burning velocity [m/s]
S_{L0}	laminar unstretched burning velocity [m/s]
S_T	turbulent flame speed [m/s]
St	stokes number
S_w	swirl number
$S_{w,l}$	local swirl number
T	temperature [K]
ti	time at index i [s]
t_0	integral time scale [s]
t_η	Kolmogorov time [s]
U	velocity [m/s]
u	axial velocity [m/s]
u'	axial rms component of the fluctuating velocity [m/s]
u_η	Kolmogorov velocity [m/s]
V	volume [m^3]
v'	transverse fluctuating velocity [m/s]
v'	vibrational level in the first excited state
v''	vibrational level in the ground state
$vol.$	volume [m^3]
Wo	Wobbe index [MJ/Nm^3]
W_{out}	work out [J]
w	angular velocity component [m/s]
$X^2\Pi$	ground electric state in the OH radical
x	length in the x direction [m]

Greek symbols

α	flame half angle
β	shift in degrees between vortices position
γ	Quarl divergent half angle
Δ	difference
ΔH	specific heat release over combustor [J/kg]
ΔT	heat release over combustor [K]
$\Delta\omega$	refraction angle
δ_T	turbulent brush thickness [m]
δ_{th}	flame thickness [m]
ϵ	strain rate [1/s]
ϵ_{cr}	critical extinction strain rate [1/s]
η	efficiency or Kolmogorov length scale [m]
$\eta_{comb.}$	combustor efficiency
η_{GT}	gas turbine efficiency
θ	loading factor as defined by Lefebvre [$\mathrm{s\,atm^{1.75}m^{2.75}/kg}$)]
κ	Stretch rate [1/s]
λ	thermal diffusivity [$\mathrm{m^2/s}$]
μ	dynamic viscosity [$\mathrm{kg/(m\,s)}$]
ν	kinematic viscosity [$\mathrm{m^2/s}$]
ρ	density [$\mathrm{kg/m^3}$]
Σ_{max}	surface density at centre of brush [1/m]
τ_{ch}	chemical time scale [s]
$\tau_{ch,cr}$	critical chemical time [s]
τ_l	local mixing time [s]
τ_η	turbulent time scale [s]
ϕ	equivalence ratio

Subscripts

C	cold
c	characteristic
ch	chemical

$comb.$	combustor
cr	critical
F	fuel
GT	gas turbine
g	gas
H	hot
p	particle
$rec.$	recirculated
ref	reference value
St	stoichiometry
T	turbulent
tot	total
1	inlet to compressor
2	inlet to combustor
3	outlet to combustor
4	outlet to turbine

Other notations

$[K]$	matrix with the covariance of the data set
$[\lambda]$	matrix with POD eigen values
$[\varphi]$	matrix with POD eigen vectors

Abbreviations

CCD	charge coupled device
CCS	carbon capture and storage
CFD	computational fluid dynamics
COT	combustor outlet temperature [K] or [°C]
DLE	dry low emission
DNG	Danish natural gas
HHV	higher heating value [MJ/kg]
LBO	lean blowout
LDA	laser doppler anemometry
LHV	lower heating value [MJ/kg]

LIF	laser induced fluorescence
PFR	plug flow reactor
PIV	particle image velocimetry
POD	proper orthogonal decomposition
PSR	perfectly stirred reactor
RPL	rich-pilot-lean
SGT	Siemens gas turbine
SIT	Siemens industrial turbomachinery
SOT	stator outlet temperature [K]

Contents

List of Figures

List of Tables

CHAPTER 1

Introduction

Throughout history, since Prometheus stole fire from the gods, mankind has been reliant on combustion. At first combustion was used to supply comfort heat and to cook. Along with cultural growth, the use of combustion has come to include different production processes and weaponry. The combustors have changed over time. Early anthropogenic combustion took place on open fireplaces. Modern combustion mostly takes place inside a closed chamber, thereby enabling exhaust gas cleaning systems that minimize the environmental impact. The exhaust gas cleaning system from modern combustion can include particle filtering, removal of sulphur dioxide, removal of nitrous oxides and Carbon Capture and Storage (CCS). In the investigations conducted in this thesis, combustion takes place inside a downscaled industrial state-of-the-art Dry Low Emissions (DLE) burner. The burner was supplied by Siemens Industrial Turbomachinery (SIT) and is their fourth generation DLE burner. Currently the full-scale burner is used in the SGT-750 gas turbine.

1.1 Background

The gas turbine community is showing increasing interest in alternative fuels for gas turbines [1]. Two strong motivators for this are that the traditional fuel, i.e. natural gas, is not carbon dioxide neutral (or renewable) and that countries do not wish to be dependent on fuels produced in areas of the world that are politically unstable. Bio-gases, such as swamp gas, landfill gas, or digester gas, are considered carbon dioxide neutral. Their constituents are dominated by methane and can be upgraded to directly replace natural gas as a fuel. Other gases of interest are bi-products from the chemical industry, coke oven gases and coal/biomass gasification gases. The gasification gases are sometimes called syngas, as they are an intermediate product in the manufacture of synthetic natural gas. However, burning these gases directly without forming synthetic natural gas will save energy. Syngas mainly comprises hydrogen, carbon monoxide and an inert (e.g. carbon dioxide or nitrogen). Technological knowledge is lacking about combustion of bio-gas and syngas, and there is known difficulties that must be addressed when creating a combustor in which these gases are to be used, such as combustion instabilities [2]. Ideally, a combustor that can handle all gases without any modifications that cause downtime is preferable. This is a daunting task for engineers.

One difficulty with these gases is that they have lower calorific value, i.e. lower energy contents per unit mass (or volume). For bio-gas, which mainly consists of diluted methane, this will increase the time needed to complete combustion. This limits the operation range, either because there will not be enough heat to sustain the reaction or because of combustion instabilities. Another difficulty (of syngas specifically) is the high hydrogen content [3]. Since hydrogen has a small molecule and reacts easily with oxygen, it is prone to cause problems such as flashback. Flashback causes the flame to move upstream where it extinguishes or attaches at an unintended position. The unintended attachment can causes serious damage to the burner, and should be avoided.

Besides complications that cause flame extinction or combustor damage, it is important to minimize pollutants. The primary pollutant from gas turbines, not including carbon dioxide, is nitrogen oxides (NO_X). In a gas turbine, NO_X emissions are primarily created in the high temper-

ature zones of the flame [4]. The highest combustion temperatures are created close to stoichiometry. For fuels with high hydrogen content the stoichiometric combustion temperature is higher than for natural gas. To avoid high-temperature combustion, the mixtures should be fuel lean or fuel rich. There is a lean/rich limit where combustion becomes unstable or the flame extinguishes. This limit will vary, not only, with gas composition but also with the properties of the specific burner.

As pressurized testing is expensive and technically difficult, limited experimental data is available, especially for unconventional fuels. Phenomena like blowout and flashback are influenced by increased pressure. This makes it important to investigate a new burner design at elevated pressures. The emissions from a burner will also change with pressure. Even though the fundamental chemistry behind the formation of emissions at different pressures are well described, the pressure influence for a specific burner is more difficult to predict. For example, reports on how NO_X emissions are affected by increasing pressure vary in literature [4-7].

In the design process of a new flexi-fuel burner, Computational Fluid Dynamics (CFD) has become an important tool. How well the CFD calculations can mimic the real combustion situation relies strongly on high quality data sets that are experimentally based. The data sets must be valid for the specific combustor and combustion case. Therefore, new data sets must be produced, not only for every new burner design but also for different fuels. After validation with the experimental data, the CFD investigations can produce a more detailed view of the fluid motions and chemistry involved in the combustion process and, to some extent, even predict what will happen when changing the premises outside the experimental data sets. The CFD results can then be used to further improve the combustor.

1.2 Objectives

The main objective of this thesis was to experimentally investigate syngas combustion, particularly gases with lower calorific value. Flashback and blowout phenomena were to be considered. A CFD validation data set (including emissions, planar OH-LIF and flow field measurements) was to be produced.

1.3 Limitations

The investigation in this thesis is limited to the gases stated in Tables 3.2 and 3.1. The tested pressures ranged from atmospheric to 9 bar. The CFD calculations presented in this thesis were performed by our partner at Chalmers University of Technology.

1.4 Methodologies

Four different experimental setups were used in this thesis, two atmospheric and two pressurized. The first atmospheric setup was built to measure the laminar flame speed of gases with varying composition using the half-angle method. Schlieren photography was used to visualize the flame. In order to obtain results that were comparable with other measurement methodologies, stretch correction was implemented [8]. Particle Image Velocimetry (PIV) was used to achieve the necessary flow field used in the stretch correction .

The second atmospheric setup was built to facilitate the full burner. Several measurement methods were used in this setup, e.g.;

- CO tracking, using infra-red spectrometry in a gas analyzer. This was specifically used during lean blowout measurements.
- NO_X emissions with varying burner parameters, using chemiluminescence in a gas analyser.
- PIV was used to measure the flow field for the various gases.
- LIF was used to measure the flame location for the various gases. These measurments were performed by the division of Combustion Physics, Lund University.
- Wall temperature measurements were used to estimate the flame location inside the RPL.

The third and fourth experimental setups were located at the DESS pressurized testing facility at the Department of Physics [9]. The third setup was aimed at investigating the central body of the burner and the fourth

setup to investigate the full burner. The methods used for the pressurized setups were the same as the atmospheric setup, excluding PIV.

In addition to the experimental methodologies, numerical methodologies were used to increase the value of the measurements, e.g.:

- Chemical Kinetics computation was used to calculate combustion properties, e.g. adiabatic flame temperature, laminar flame speed, lean blowout, reaction pathways.

- Proper Orthogonal Decomposition (POD) was used on the PIV velocity field and the CFD velocity field to increase the value of the data used to validate CFD calculations. The POD was also used to visualize specific features of the flow field.

1.5 Outline of thesis

This thesis comprises five chapters that provide a framework to the reader about the attached papers. Nine papers are attached to the end of this thesis.

Chapter 1
Introduction, in which the background and inspiration for this work are described.

Chapter 2
Gas turbine combustor, introduces the gas turbine cycle in which the operating conditions for a combustor are discussed. This chapter also describes important considerations for the design of a combustor with emphasis on the presented combustor.

Chapter 3
Experimental setups, supplements the papers with more information about the experimental setups used. (Some of the information in this chapter can also be found in the attached papers.)

Chapter 4
Diagnostic methods, describes the optical experimental methods used in the papers, e.g. PIV, OH-LIF and Schlieren imaging. (Some of the information in this chapter can also be found in the attached papers.)

Chapter 5
Combustor theory – Combustion chemistry and fluid dynamics in a swirl combustor; this chapter gives an overview of the combustion phenomena encountered during the course of this thesis. A selection of results, from the papers concerning the various phenomena is shown. (Some of the information in this chapter can also be found in the attached papers.)

CHAPTER 2

Gas Turbine Combustor

To understand the conditions under which a gas turbine combustor must operate, there must be an understanding of the components surrounding the combustor. The gas turbine consists of three main parts (Figure 2.1). The first part is the compressor, which draws air into the gas turbine, adds energy to the air via a rotating shaft and increases the air pressure [10]. The second part is the combustor, in which fuel is added to the air stream; the temperature is subsequently raised by releasing the chemical energy in the fuel. In the gas turbine, the exhaust is expanded to a lower pressure [11]. During the expansion, energy in the gas stream is transferred to the gas turbine shaft. In a single-shaft engine [12], the turbine expander and the compressor are on the same shaft. Depending on the purpose of the gas turbine, this shaft can be connected to an external system, such as mechanical shaft power for driving propellers on ships, or electrical power via a generator. In aircraft, the gas turbine is used to produce propulsion power. The gas turbine cycle is also called the Brayton cycle, after the engineer George Brayton. A thermodynamic understanding of the cycle can be obtained by studying the T-s diagram

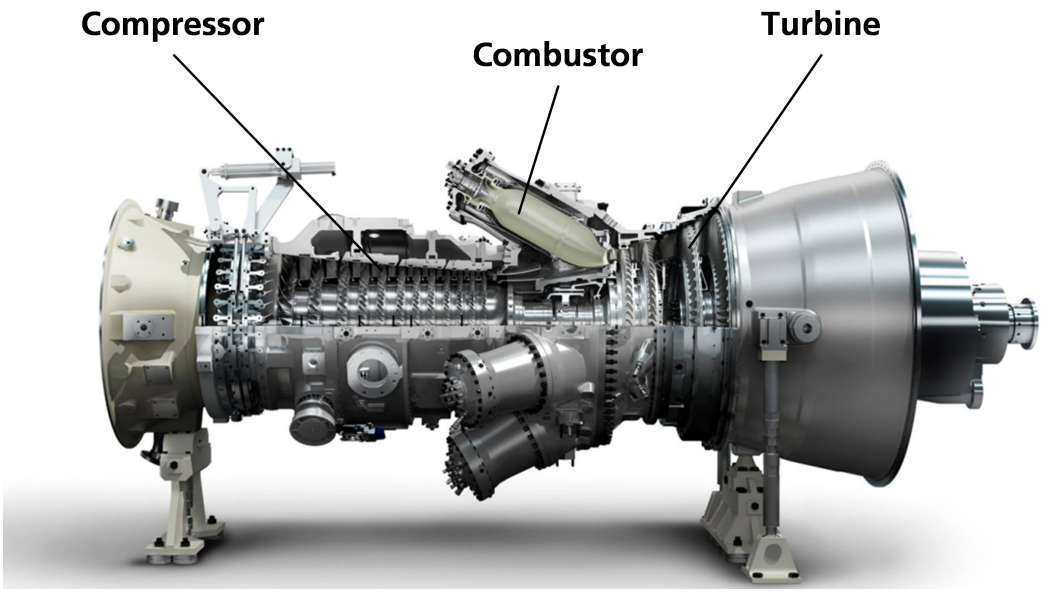

Figure 2.1: The SIT gas turbine, SGT-750, in which the full-scale version of the combustor investigated in this thesis operates. (Courtesy of Siemens Industrial Turbomachinery [SIT].)

(Figure 2.2).

In the ideal Brayton cycle diagram, Figure 2.2, it can be seen that the temperature is increased from position 1 to position 2 because of the isentropic compression of the gas by the ideal compressor. Heat is then added via combustion at constant pressure, thereby further increasing the temperature. The expander then reduces the pressure from P_2 to P_1 and the temperature drops. The area inside the cycle in the T-S diagram equals the work output of the cycle. The efficiency of the cycle equals the work done divided by the heat input (2.1).

$$\eta_{GT} = \frac{W_{out}}{Q_{in}}, \tag{2.1}$$

Maximizing work output can be achieved by maximizing the area of the Brayton cycle (Figure 2.2). This can be done by maximizing the difference

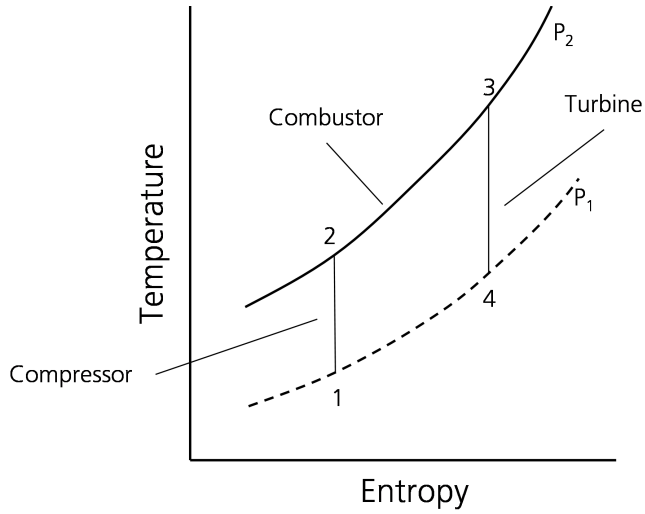

Figure 2.2: Temperature entropy diagram for the Brayton cycle.

between the lowest and highest temperatures while increasing the pressure ratio. Since the lowest temperature of the system is limited by the surrounding temperature and pressure, and the maximum temperature is limited by the combustor temperature there is a maximum theoretical efficiency of the cycle. This efficiency is called the Carnot efficiency (2.2).

$$\eta_{Carnot} = 1 - \frac{T_C}{T_H}, \tag{2.2}$$

This ideal theoretical efficiency cannot be achieved since the isobars in the t-s diagram are not isothermal. There will also be mechanical, fluid dynamic and thermodynamic losses. In a real cycle, (here the discussion is limited to single cycle), the Carnot efficiency is not the best way to describe optimal thermal efficiency. Walsh and Fletcher [12] state that the optimum thermal efficiency is reached when the temperature increase over the combustor is low compared to the temperature after the turbine. Increasing the pressure at a constant temperature would then force the cycle towards a Carnot cycle. Since the highest cycle temperature is often limited by the material and cooling of the first turbine stages, pressure

ratio can be optimized to maximize the efficiency for a specific combustor temperature [12]. Besides optimization of the efficiency, the gas turbine should be optimized for the power output (Figure 2.3). The optimization sets the conditions for the combustor. For the gas turbine cycle in Figure 2.3 at a combustor outlet temperature (COT) at 1743 K, the optimal pressure ratio for specific power is 14.3 bar and the optimal pressure ratio for efficiency is 25.1 bar. These values are engine-specific but show the tendency for optimization.

Today, single-cycle efficiency above 40 % for smaller engines are common and, for heavy frame engines, efficiencies above 60 % are available [1]. Modern gas turbines have a COT of 1800 K for the heavy frame engine (up to ∼300 MW), and 1700 K for the midrange engines (∼100 MW) [1]. The COT temperature is being pushed towards 1900 K [13]; this will be a challenge for DLE combustors as the thermal NO_X will increase significantly above around 1850 K [14]. Consequently, maintaining low NO_X emission while having high efficiency is contradictory.

In order to minimize NO_X emissions, the combustion temperatures are being pushed towards lower temperatures. This means that achieving ultra-low NO_X emissions will have a negative influence on cycle efficiency. In this thesis, the experimental work is largely limited to atmospheric condition and maximum temperatures around 1750 K.

2.1 The combustor

2.1.1 General combustors

The purpose of a combustor is to transform chemically bound energy to heat, in order to increase the temperature before the turbine. The arrangement for a combustor section varies for different gas turbines. For example, many combustors may be placed in an annular arrangement surrounding the gas turbine, or just a single larger combustor on the side of the gas turbine [12,14]. The annular arrangement could consist of separate cans or could be placed in an open chamber. The combustion zone (Figure 2.4) is similar for all the combustors mentioned previously. First, there is a primary zone where combustion is initiated. Here the

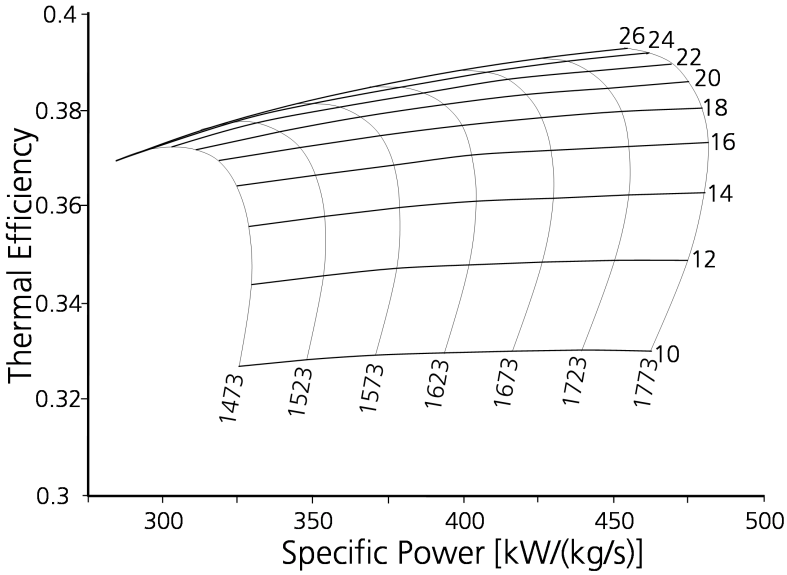

Figure 2.3: Thermal efficiency vs Specific power for varying pressure ratios (10- 26) and COT (1473- 1773 K) for a gas turbine. At 1643 K the thermal efficiency is optimized at pressure ratio 25.1 and the specific power is optimized at pressure ratio 14.3 [15].

flame is anchored, e.g. by bluff body stabilization [16] or by a swirl flow [17]. Next is the secondary zone, where more air is supplied to complete combustion, and finally the dilution zone, where excess air is added to attain the final combustor exit temperature. Usually, along the walls of a combustor, the liner, cooling air is impinged to reduce the wall temperature and prolong the lifetime of the liner.

2.1.2 The investigated combustor

The investigated burner, which is a fourth generation DLE burner in Siemens' development line [18-20], is only investigated in the primary

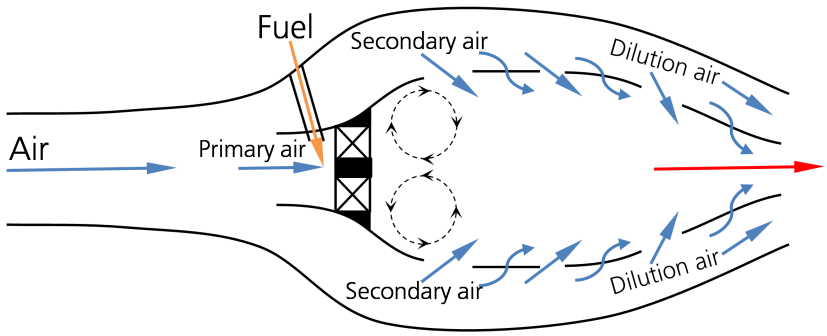

Figure 2.4: Schematic illustration of a general combustor.

zone, and no cooling air or dilution air is supplied to the combustion. Prior to the primary combustion zone, this burner consists of three concentric sections (Figure 2.5). The first section is the RPL (Rich-Pilot-Lean). It is a central body pre-combustor and can be operated from fuel lean to fuel rich conditions. The choice of lean or rich conditions for the RPL can be optimized to satisfy combustion stability concerns [21] and to minimize NO_X emissions [22]. The purpose of the RPL is to supply heat and radicals to the other burner sections. The second burner section, the pilot, serves as an intermediate link between the RPL and the Main section, in which the fuel flow can be adjusted to ensure combustion stability. The third section, the Main, is where most fuel and air is supplied (79 %). All three combustors have their own swirler. After the burner configuration, there is a throat followed by the Quarl (Figure 2.5). The Quarl is a diffuser that has several positive effects. Most easily understood is the expansion effect that lowers the velocity that lowers the total pressure drop through the burner [14]. Another reason, specifically for swirl stabilized burners, is that the Quarl causes the recirculated mass flow to be higher than for burners with a straight nozzle (sudden expansion) for the same swirl number (Figure 2.6) [17,23]. In this thesis, the burner section up to and including the Quarl section was supplied by SIT. The downstream section, the liner, was designed to achieve high combustor efficiency.

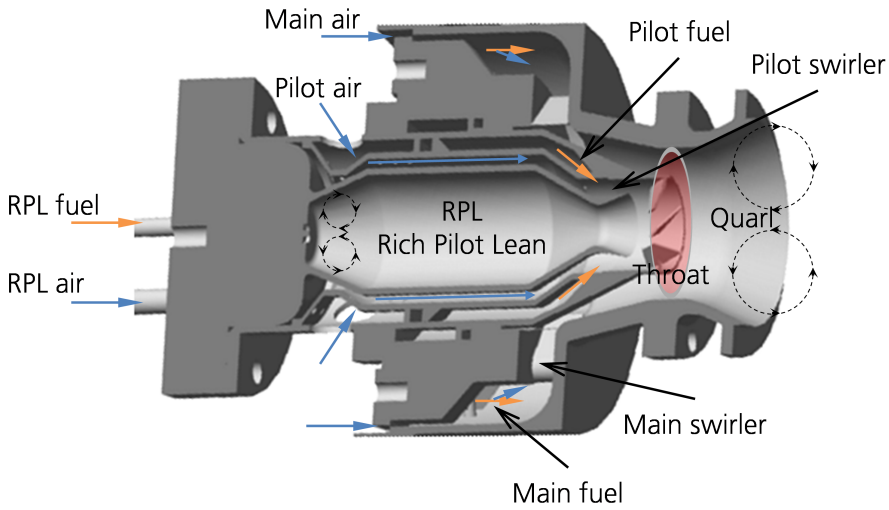

Figure 2.5: Cross section of the SIT burner with recirculation zones. The main section has a radial swirler and the pilot has an axial swirler.

2.1.3 Combustor loading

Figure 2.7 shows how the combustion efficiency varies with combustor loading. As a guideline, the liner was designed to achieve a combustor loading (2.3) below 10 kg/(s atm$^{1.8}$m^3), according to guidelines from Walsh and Fletcher [12].

$$CL = \frac{\dot{m}}{VP^{1.8}10^{0.00145(T_3-400)}}, \tag{2.3}$$

The strength of using combustor loading as a predictor for combustion efficiency can be seen by analysing the θ factor derived by Lefebvre (2.4) [14]. The combustor loading and the θ factor are approximately inversely

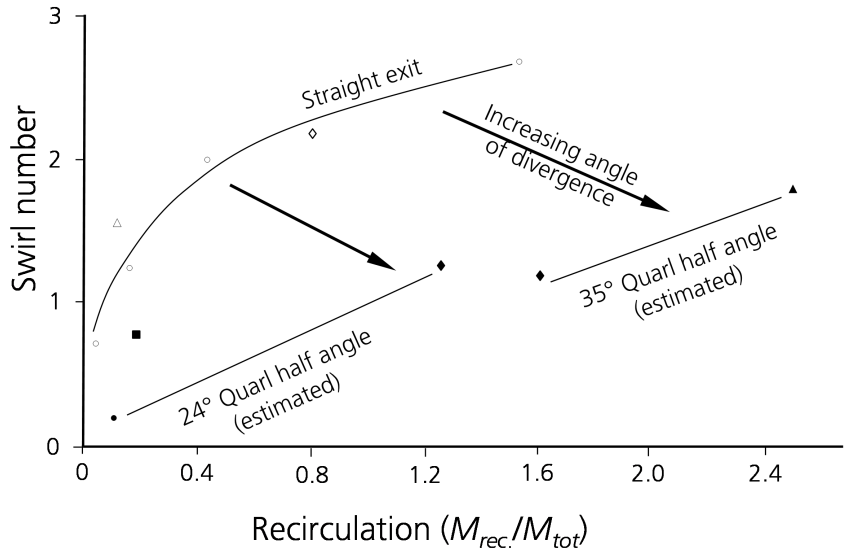

Figure 2.6: Variation of recirculated mass flow with swirl number, adapted from Syred and Beér [17]. Straight exit: ○ Martur and MacCallum [24], △ Chigier and Beér [25], ◊ Syred, Chigier and Beér [26]. Diverging angle (γ): ● γ=24° Chigier and Gilbert [27], ▲ γ=35° Dvorak [17], ♦ γ=21.5° and 31.5° Smithson [28], ■ γ=25° Sigfrid et al. [23].

proportional to each other.

$$\theta = \frac{P_{in}^{1.75} A_{ref} D_{ref}^{0.75} e^{\frac{T_{in}}{300}}}{\dot{m}}, \tag{2.4}$$

The combustor loading factor is based on empirical work collected by Walsh and Fletcher [12] and the θ factor has been derived from combustor efficiency [14, 29]. Lefebvre assumed that the combustor efficiency can be calculated by assuming that the combustion heat release is proportional to the area of the flame, the temperature increase and the turbulent flame speed (2.5).

$$\eta_{comb.} = \frac{\Delta H_{comb.}}{H_F} = \frac{\rho_g A_f S_T c_P \Delta T}{q \dot{m}_A H}, \tag{2.5}$$

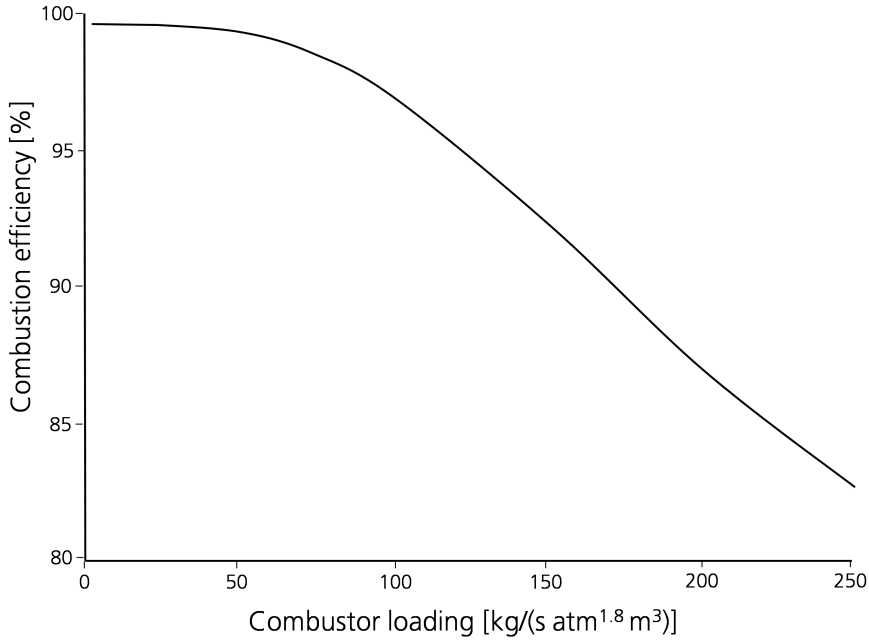

Figure 2.7: Illustration of combustion efficiency as function of combustor (adapted from Walsh and Fletcher [12]).

Two important assumptions are made in order to reach the final expression. The first is how the turbulent flame speed relates to the laminar flame speed (5.28) [29]. The second is how the laminar flame speed change with pressure and temperature (2.7) [29].

$$S_T \sim \sqrt{2 S_L R e^a u'}, \tag{2.6}$$

$$S_L \sim P^{\frac{n-2}{2}} f(T), \tag{2.7}$$

The root mean square value of the fluctuating velocity is assumed to be proportional to the pressure drop over the combustor and the dynamic viscosity proportional to $T^{0.7}$. The resulting equation is (2.8) [14,29] :

$$\eta_{comb.} = f(\theta) = f\left(\frac{P_{in}^{\frac{n}{2(1-a)}} A_{ref} D_{ref}^{\frac{a}{1-a}} e^{\frac{T_{in}}{300}}}{\dot{m}} \right), \tag{2.8}$$

By setting the reaction order, n, to 2 and the Reynolds exponent, a, to 0.5, the same θ factor as defined in Equation 2.4 is found. This equation has been found to correlate well with experimental data [14]. In order to get good correlation with syngas, it may be necessary to choose different exponents in Equation 2.8. However, as syngas fuels have a higher laminar flame speed, there should be no negative influence on combustion efficiency by using the existing design parameters. For fuels with lower flame speed than methane, this design procedure might overestimate the combustion efficiency of a burner when using these fuels. To compensate for the lower burning velocities for fuels as diluted methane it is necessary to have a long residence time in the liner. The length of the liner used in this thesis was designed to give a residence time above 10 ms. The residence time was chosen to fulfill SIT specifications. Walsh and Fletcher [12] states that the minimum time should be minimum 3 ms for conventional combustors.

CHAPTER 3

Experimental setups

The goal of the thesis was to experimentally examine how an industrial burner handles a range of fuels from the standard fuel, e.g. natural gas, to low calorific gases and syngas containing hydrogen and carbon monoxide. To facilitate the experimental investigations four separate experimental setups was created. The setups were:

1. The laminar flame speed setup [30]
2. The atmospheric full burner setup [21-23]
3. The pressurized central body burner (RPL) setup [31, 32]
4. The pressurized full burner setup [31]

The descriptions of the different setups in the sections below are written to supplement the descriptions of the setups in the presented publications [21-23, 30-32]. Some of the information in this chapter can also be found in the presented publications.

3.1 The laminar flame speed setup

The laminar flame speed for a range of fuels was investigated, to obtain a better understanding of how well different fuels burn (Table 3.1). The experimental methodology for measuring the flame speed was based on the half-angle method [33]. This method uses the measured half-angle of the flame (Figure 3.1) to calculate the flame speed (3.1).

$$S_L = u \sin \alpha, \tag{3.1}$$

The flame angle was obtained by locating the flame edge using a Schlieren

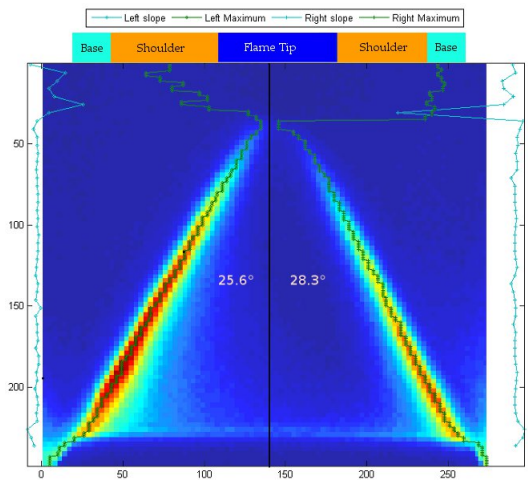

Figure 3.1: Flame half-angles before correction for camera misalignment [30].

set up. The Schlieren measurement technique is described in Chapter 5.

The burner used in the experiments was of Bunsen-burner type, where the fuel and air was mixed before entering the bottom of a 500 mm tube. The tube converged to the exit diameter. The exit of the burner was adjustable, by use of three different exit nozzles, to ensure stable combustion and to avoid flashback. The exit diameters used were 13 mm, 10 mm and 4 mm. The larger diameter was needed to measure lower lam-

Table 3.1: Gas composition for laminar flame experiments [30]

Gases	Gas compositions vol.%				Wo*	LHV
	CH_4	H_2	CO	CO_2	[MJ/Nm^3]	[MJ/kg]
Methane	100	0	0	0	55.30	50.01
A1	10	45	45	0	21.71	20.93
A2	10	67.5	22.5	0	27.70	33.14
B1	64.4	0	0	35.6	28.15	19.87
B2	60.06	5.08	0	35.32	27.51	19.65
B3	57.2	10.6	0	32.74	27.60	20.36

* Wobbe index based on the higher heating value (HHV).

inar flame speeds and the smaller size was needed for the higher flame speeds. The 10 mm nozzle was used for the reference gas, methane.

The measurements were performed at both room temperature, 25 °C, and at 270 °C. The burner tube was placed inside an insulated resistive coil heater that was used to heat the fuel and air mixture to 270 °C. The temperature was measured at the nozzle exit plane before and after the measurements, and any temperature variations greater than 5 °C were disregarded. The fuel and air flows were measured using Bronkhorst thermal mass flow controllers.

3.2 The atmospheric full burner setup

The atmospheric setup was based on a dual fan system with individual thermal flow meters and heaters (Figures 3.2 to 3.4). The fan system supplied air to the Main and Pilot sections of the burner. The setup also included fuel mass flow controllers, one for each burner section, and a separate mass flow controller for the RPL air. The RPL air was heated with the same resistive coil heater as for the laminar flame speed measurements. To heat the RPL air, a coiled pipe section was placed inside the heater which transferred the heat to the air passing through the pipe.

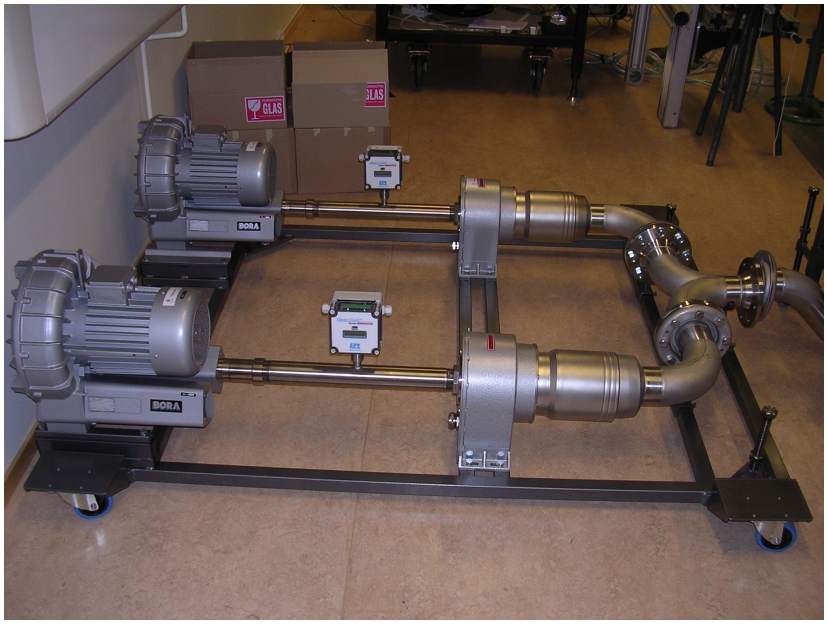

Figure 3.2: The dual fan system with heaters and flow meters.

Before a vertical straight pipe leading to the burner, the Main and Pilot air coming from the dual fan system takes a 90° bend. To minimize secondary flow and to achieve a more even flow profile, the set up included two 10 cm flow straighteners consisting of a square tube matrix. The flow straighteners were placed both in the bottom pipe and in the connection pipe leading up to the burner section. The vertical pipe section leading to the burner was equipped with connections for temperature measurements, pressure measurements and injectors for PIV particles. The seeding injector air flow was controlled separately with a needle valve, and measured using a Coriolis mass flow meter.

After the burner, three different alternative liners could be interchangeably connected. The first liner, which was used for the atmospheric emissions and lean blowout publications [21,22], was a 700 mm long stainless steel pipe with a 85 mm diameter which contracted to a diameter of 50 mm at the end (Figure 3.3). After the contraction, a pipe extended a

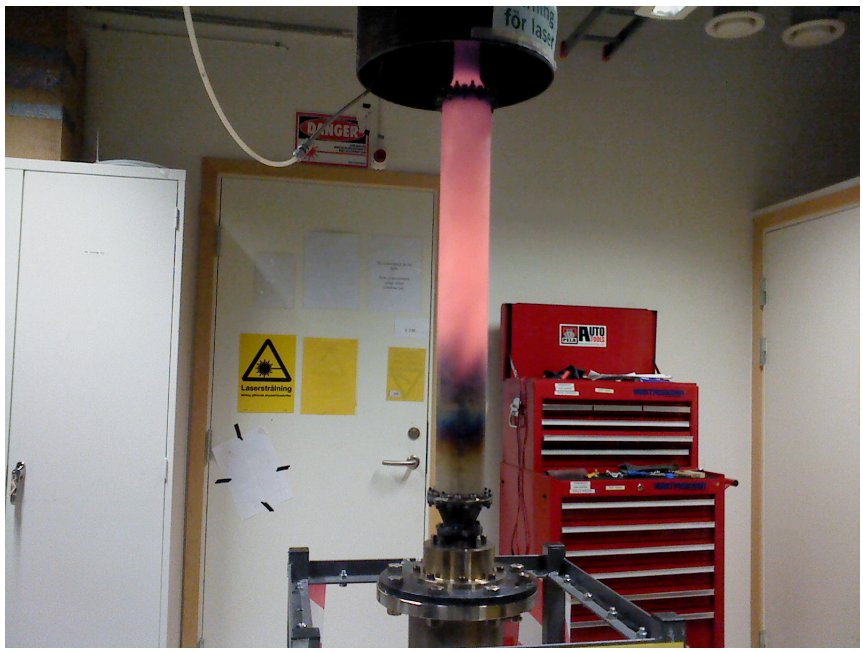

Figure 3.3: The liner after the burner was glowing orange due to the hot combustion gases.

further 150 mm. Fifty mm from the 150 mm pipe end there was a connection for an emission probe. The emissions probe was a 5 mm closed-end pipe with 8 equidistant holes placed at the wake side of the pipe. As the pipe was not cooled, several probe pipes were manufactured, so that they could be changed as they got burnt.

The second and third liners were made of two parts. The lower part was made of quartz, enabling the use of different optical diagnostic techniques, e.g. PIV and OH-LIF. The upper part was an extension made of stainless steel and ensured that the length of the liner was the same as for the full stainless steel liners.

The measurements in the atmospheric setup were conducted with preheated air at 650 K. The gases that were tested are listed in Table 3.2. The syngas with high hydrogen content had a characteristic white flame (Figure 3.5).

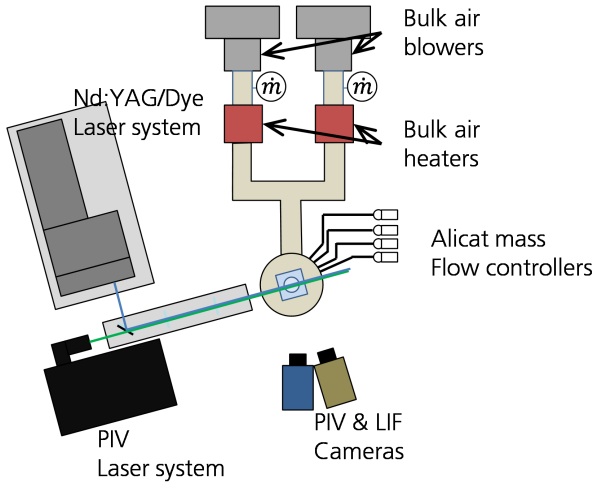

Figure 3.4: Setup for the atmospheric experiments. The setup facilitated laser techniques, e.g. PIV and OH-LIF. At the exit of the liner, the setup could be connected to an emission measurement rack.

Table 3.2: Gas composition for the atmospheric burner experiments [21,22]

Gases	Gas compositions vol.%				Wo*	LHV	$Fuel/Air_{St}$
	CH_4	H_2	CO	N_2	[MJ/Nm^3]	[MJ/kg]	
Methane	100	0	0	0	55.3	50.0	0.058
Dil. Methane	33.5	0	0	66.5	15.0	11.2	0.26
Syngas	10	67.5	22.5	0	27.7	33.1	0.10
Dil. Syngas	6.9	46.6	15.5	31.0	15.0	14.1	0.25

* Wobbe index based on the higher heating value (HHV).

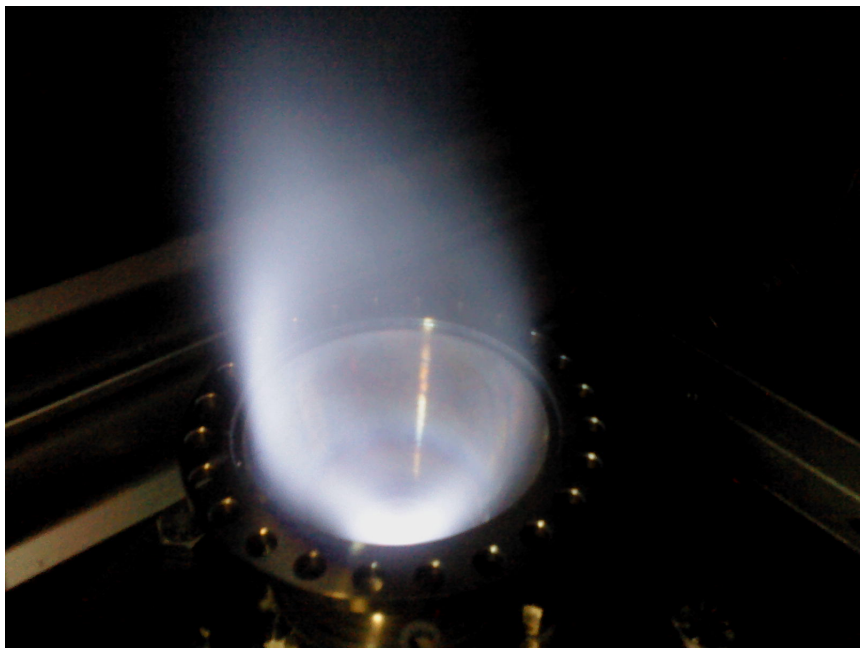

Figure 3.5: Combustion of syngas without the liner. The white flame distinguished the syngas flame from the blue methane flame. The asymmetrical shape of the flame in this image was caused by a blocked fuel hole. The fuel holes were cleaned before measurements.

3.3 The pressurized central body burner setup

All pressurized experiments in this thesis were carried out at the high pressure facility at Lund University [9]. To ensure mounting of the central body burner (the RPL) at the high pressure, a connection piece was constructed (Figure 3.6). The connection piece was made up of two cylindrical sections. The first section had 6 large holes around the circumference. This section was connected to the RPL bottom plate.

The second section was welded onto the outer shell with 1 mm cooling holes drilled to supply impingement cooling to the bottom part of the RPL. The cooling air then continued along the RPL body and was dumped 10 mm before the RPL exit. The RPL fuel and air was sup-

plied using gas bottles, measured using Coriolis mass flow meters and controlled using needle valves. The air flow was heated with the same heating system that was used for the atmospheric setup. The flame inside the RPL was ignited using a spark plug placed in the bottom of the RPL. The RPL could be ignited with the igniter for all fuels at all tested pressures.

Figure 3.6: The connection piece for the high pressure facility. To the left, the two sections of the connection piece are placed next to each other and show the distribution holes for cooling of the RPL. To the right, the two sections are welded together.

The RPL connection piece was mounted to the liner of the high pressure facility in the plenum (Figure 3.7). The liner, after the burner, had a square cross section with the dimensions $100 \times 100 \times 135$ mm. The liner was equipped with quartz windows for laser diagnostics. After the liner, there was a step-contraction to a 60 mm cylindrical section. In this section, temperature could be measured or emission samples taken. After the cylindrical section, there was a water cooled pressure regulating valve. The exhaust gases were then cooled by water sprays and led out to the atmosphere.

The measurements in the pressurized central burner setup were conducted with preheated air, at 650 K. The gases tested in this investigation were the same as in the atmospheric experiments (Table 3.2). The pressures were 3, 6 and 9 bar.

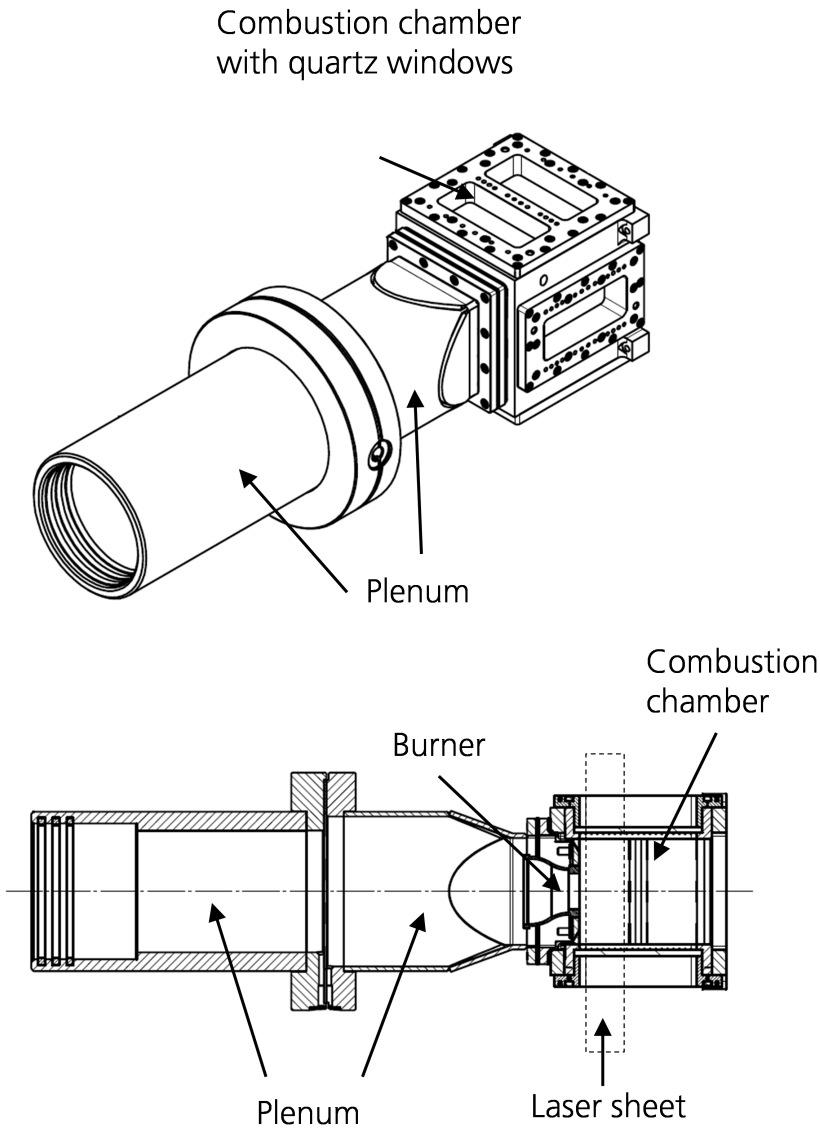

Figure 3.7: The RPL burner was connected to the plenum of the high pressure facility via a connection piece. The combustion chamber was equipped with quartz windows to facilitate laser diagnostics [34].

3.4 The pressurized full burner setup

As the full burner did not fit the original plenum (Figure 3.7), the high pressure facility was modified. A new plenum was built to fit the full burner (Figure 3.8). In addition the liner section was expanded to ensure a sufficiently long residence time for complete combustion to be achieved, i.e. approximately 15 ms, and a combustor loading below $10\,\mathrm{kg/s\,atm^{1.8}m^3}$. The square section of the liner was still $100\times100\,\mathrm{mm}$, but the length was now 459 mm. The optical access was the same as for the previous design, with the addition of a second optical access possibility downstream of the first section (Figure 3.8). Cooling air was channelled along the outside wall of the liner in order to avoid overheating of the liner. This kept the liner outer wall temperature close to 300 °C during combustion.

The air was supplied to the Main and Pilot sections by the air compressor

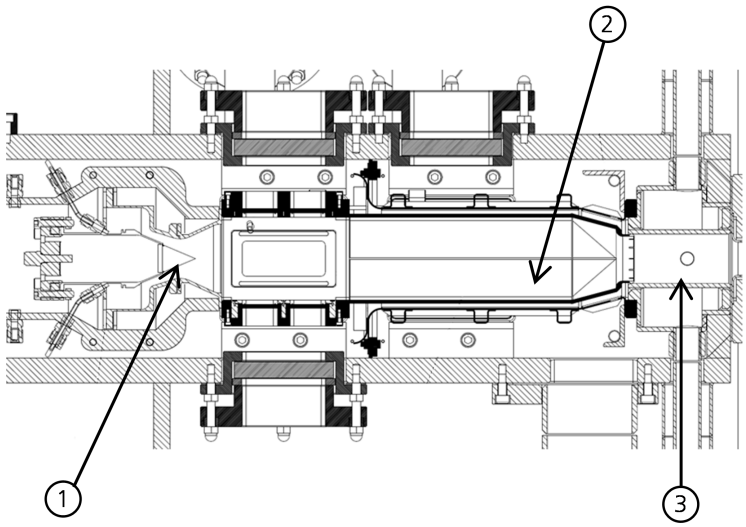

Figure 3.8: The new plenum and test section, 1: DLE burner; 2: Liner with quartz windows; 3 Emission probe position.

system of the high pressure facility. It was heated before the combustion

chamber in a heating tower to a preheat temperature of 650 K. An external system was built to supply fuel and RPL air to the burner (Figure 3.9). Air and methane were supplied to the RPL section and preheated in the same manner as for the pressurized central burner setup. The fuel, Danish natural gas (DNG), was supplied to the Pilot and the Main burner sections from the city natural gas grid via the gas compressor system of the high pressure facility. Nitrogen was added to the DNG to change the heating value of the fuel, and mixed before the fuel gas flow was led to the respective burner sections (Figure 3.9). The mass flows were measured using coriolis mass flow meters and controlled by manual needle valves.

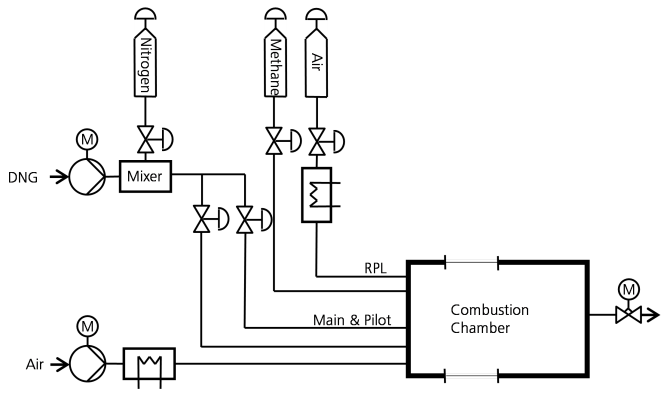

Figure 3.9: High pressure facility flow chart.

The lead to the spark plug had to be rebuilt because the air to the Main and Pilot was preheated above lead temperature limit. This was done by replacing the original insulation material in the plug connector with cast ceramic paste and replacing the lead insulation with two layers of ceramic beads (Figure 3.10).

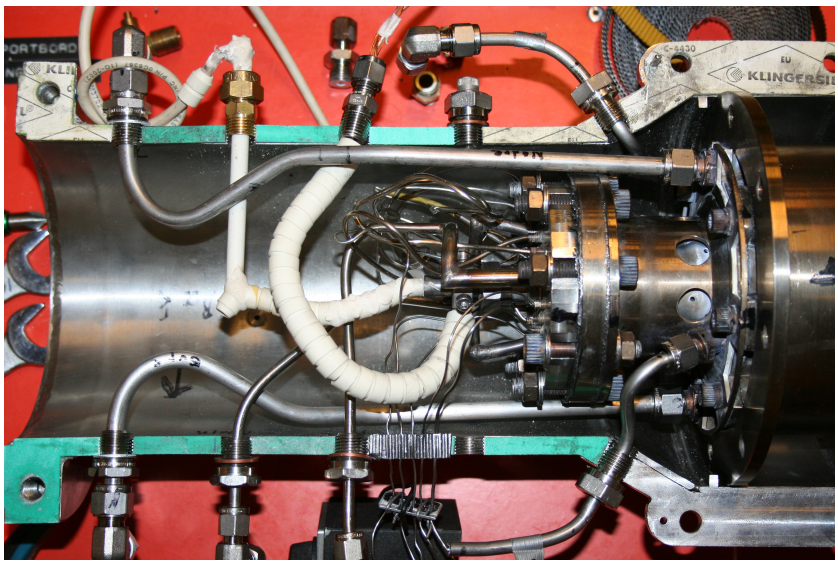

Figure 3.10: The new plenum for the DLE high pressure facility experiments. The ceramic beads insulate the igniter lead.

The measurements in the pressurized full burner setup were conducted with preheated air of 650 K. The gas tested was natural gas diluted with nitrogen to Wobbe index 40 MJ/m^3 and 30 MJ/m^3. The pressures were 3, 4.5 and 6 bar.

CHAPTER 4

Diagnostic methods

Several measurement methods were used in this thesis. The methods ranged from thermocouple measurements to advanced laser-based methods. In this chapter, the optical methods will be described. The diagnostic methods described here are Particle Image Velocimetry (PIV), Laser Induced Florescence (LIF) and Schlieren imaging.

4.1 Particle Image Velocimetry

The performance of gas turbine combustion is determined by the combination of chemical kinetic and fluid dynamic interactions. Consequently, the combustion phenomena are controlled and optimized not only by pure chemical interactions of species but also by how the fluid mechanics allow or limit these chemical interactions to take place. In order to identify the interaction between chemistry and fluid dynamics, it is important to be measure the fluid motion of the combustion zone. This can be done by using optical techniques such as PIV [35]. PIV gives an instantaneous two-dimensional image of the flow field (Figure 4.1). In this section, the PIV methodology will be reviewed, starting from choice

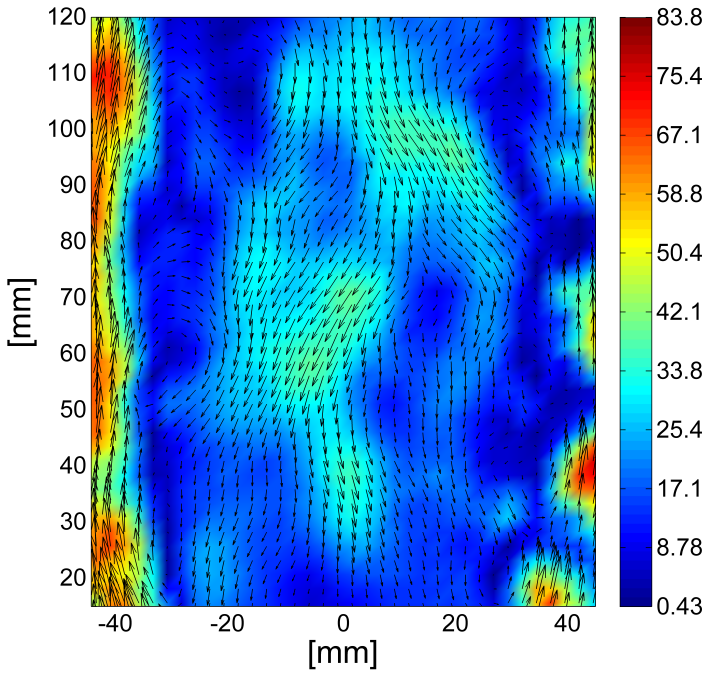

Figure 4.1: Single shot PIV images showing the recirculation zone. The colour bar show velocities in m/s. The image originates from the data set produced for paper IV [23].

of seeding and advancing to post-processing of the measured flow field.

Even if PIV is considered a non-intrusive method, it relies on seeding particles being introduced to the flow. These particles will be illuminated by a laser sheet and the light that approaches the particles will scatter, via Mie scattering [36], and the scattered light is recorded by a camera. Mie scattering is dependent on the size of the particles. Larger particles will scatter light more than smaller. There is a trade off between the intensity of the scattered light and the ability of the particles to follow the flow. The ability of the particles to follow the flow can be characterized with

the Stokes number (4.1).

$$St = d_p^2 \frac{\rho_p u_c}{18 \mu d_c}, \tag{4.1}$$

Samimy [37] showed, in a compressible free shear layer flow, that a Stokes number of 0.2 gives an error in the measured velocity of about 2 %. For flow visualization he recommends a Stokes number below 0.05. The Stokes number in this thesis is approximately 1×10^{-4} [23]. For combustion cases, the seeding particles should not only scatter light and follow the flow, they should also not be consumed in the hot flame. For these reasons, TiO_2 was chosen as seeding. The melting point for the TiO_2 seeding was 1840 °C.

After camera and laser alignment (Figure 3.4), the raw images are produced that will be used for the flow field calculations. For every flow field two images, a pair, are used (Figure 4.1). The two images are taken with a specified time delay in between. As a rule of thumb the particles should move 1/4 of an interrogation window between an image pair [38]. Interrogation windows are small subsections of the camera image representing the divisions of the original image (Figure 4.1). Each interrogation window will produce one vector. In Figure 4.1, the direction of the flow can be easily seen. This is not the case in real PIV images. The number of interrogation windows and image pairs will also be too large for a manual procedure. Mathematical correlation between the interrogation windows from the first image and the second image will be used instead. The interrogation windows in the second image is shifted in all directions in order to maximize the correlation. The direction and length of the interrogation window shift that gives the highest correlation is used to calculate the vector. There are several methods of increasing the correlation. Displacement and deformation of the second interrogation window in relation to the first are examples of how the correlation can be increased [38]. Finding the correct displacement of the second interrogation window is usually done by using the results from previous vector calculations in a multi-pass scheme to estimate the displacement [39]. In a multi-pass scheme the correlation is first calculated with a larger interrogation window and then the window size is decreased. The interrogation windows can also be overlapped in order to increase the

number of vectors and, to some extent, increase the spatial resolution of the measurement.

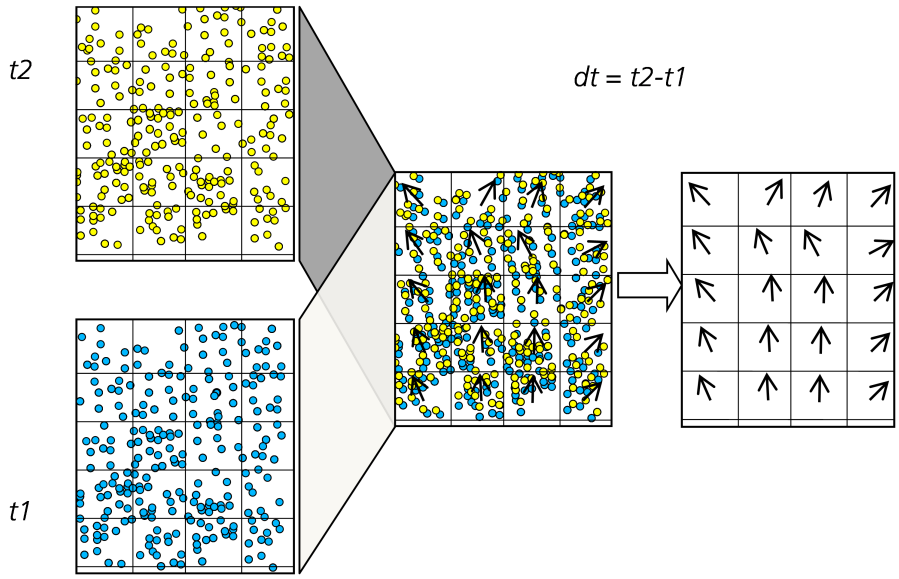

Figure 4.2: Illustration of how a PIV image pair is used to produce a flow vector field. *t1* is the time at which the first image is taken and *t2* is the time at which the second image is taken. *dt* is the time delay between the two images.

If the scattered light from the particles occupy less than one pixel on the CCD, a phenomenon called peak locking occurs. This causes the location of centre of the particle to be estimated at the centre of the pixel and the accuracy of the movement of the particle is limited by the pixel size. If the particle scattering occupies a few pixels, then interpolation schemes can be used to achieve sub-pixel accuracy of the movement [40]. Once a set of vector fields have been produced, a large range of post-processing alternatives are available. Typically the mean and fluctuating (root mean squared) velocity fields can be produced. These can easily be used as validation for CFD calculations [41-43]. In appendix A, post processing using proper orthogonal decomposition (POD) is described.

4.2 OH-Laser Induced Fluorescence

Laser induced fluorescence is when a laser is used to excite electrons of an atom or a molecule from a lower energy level to a higher energy level. The transition between these discrete levels occur when a photon with energy/wavelength corresponding to the a specific transition is absorbed by the atom or molecule. In order to choose a specific transition a tunable laser source is needed. In this thesis a Nd:YAG pump laser exciting the Rhodamine 6G gain medium of a dye laser, is used to tune the laser to the resonance wavelength of the chosen transition (Figure 5.14). The transition wavelengths are specific for different species. This makes it possible to target a specific species, such as the hydroxyl radical (OH).

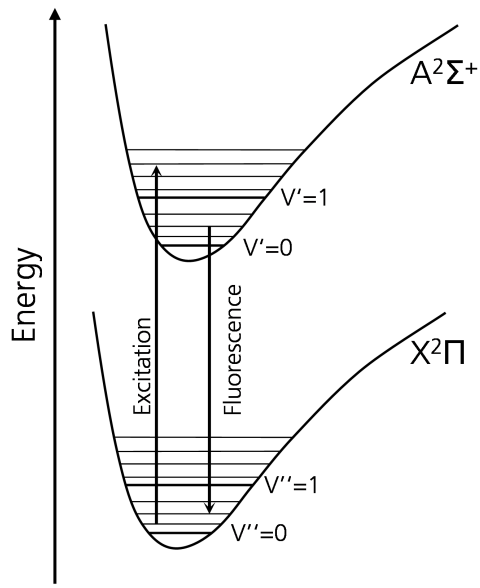

Figure 4.3: Schematic energy level diagram for the Q1(8) transition of the OH radical. The laser excitation wave length is close to 283 nm and the corresponding fluorescence signal is close to 308 nm.

Fluorescence is a spontaneous emission of radiation from the upper energy level [44]. This occurs since electrons strive to return to their

ground state, which is the state with the lowest possible energy. The fluorescent signal is usually Stokes shifted, meaning that the wavelength of the emission is longer than the absorption wavelength. This makes it possible to filter out the laser light and get a fluorescence signal that is not disturbed by the laser reflections.

For fuels containing hydrogen, e.g. syngas and hydrocarbon-based fuels, OH is one of the most important radicals for flame propagation [45-46]. In Papers I-VI, OH is used as a flame tracer as it is formed in the flame front with high temperature and exists for some time in relatively large concentrations. In combination with beneficial spectroscopic properties, this has led to the OH radical often being used as a combustion tracer (showing flame and post-flame regions) when using LIF [47]. In our experiments the OH radicals are excited through the Q1(8) transition in the $v'' = 0 \rightarrow v' = 1$ band of the $A^2\Sigma^+ \leftarrow X^2\Pi$ system by using a laser wave length close to 283 nm (Figure 4.3). This excitation is chosen because it has a strong signal and it is insensitive to temperature within the range 1400 K to 2100 K [48]. The corresponding fluorescence signal is close to 308 nm [49].

4.3 Schlieren imaging

The principle of the Schlieren method is that light passing through a media with a different density will be refracted. This is because the density variations affect the refraction index. Increasing the density increases the refraction index. The light will be refracted towards the direction of increasing index of refraction. This means that the light is bent towards the region of higher density [50]. By blocking out the part of the light that has not been refracted, an image consisting only of refracted light can be created. The refraction is proportional to the density gradient [51](4.2).

$$\Delta\omega \sim \frac{d\rho}{dx}, \tag{4.2}$$

The Schlieren setup used in this thesis was built in a "Z" arrangement (Figure 4.4). A point light source was created with a goose neck lamp and an Iris. The point source originating from the Iris opening was placed at the focal point of the first mirror. The light formed a parallel light

beam between the mirrors (Figure 4.4). The object of interest, in our case a flame, was placed in the centre of the beam. The second mirror directed the light beam into the camera via a second focal point. At the focal point the light was partly blocked out to create the Schlieren image. Blocking out the light from the top resulted in the Schlieren image in Figure 4.5.

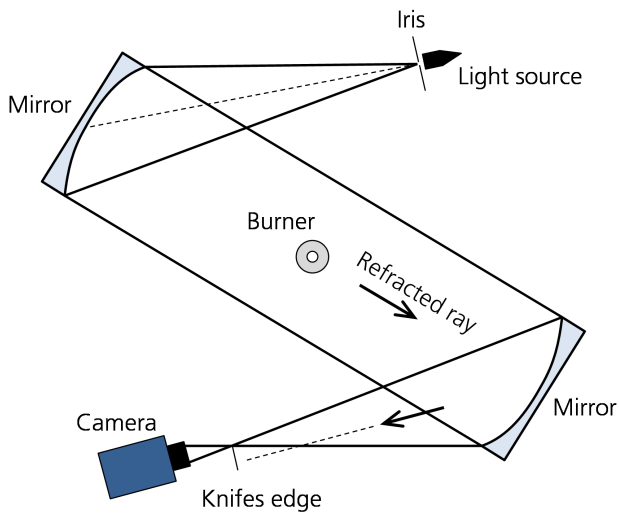

Figure 4.4: Schlieren set up using two mirrors and a light source.

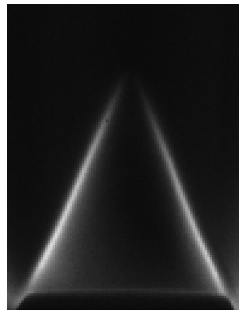

Figure 4.5: Schlieren image for methane at equivalence ratio 1.

CHAPTER 5

Combustor theory – Combustion chemistry and fluid dynamics in a premixed swirl combustor

The chemistry and fluid dynamics in gas turbine combustion are coupled in the sense that they interact with each other. Without combustion, the flow field would be different and with a different flow field the combustion process would be affected. However, the two can be decoupled to a certain extent. In the perfectly stirred region (Figure 5.1), turbulence creates a homogeneous mixture of the burnt and fresh gases. This reduces the physics of combustion to a chemically-governed phenomenon. In other regions, like the laminar, region the fluid dynamics can be simplified but there is still an interaction between chemistry and fluid dynamics. In order to estimate the regime in which the combustion will take place, the Borghi diagram can be used [52]. In this chapter, the Borghi diagram, some combustion chemistry, two coupled combustion phenomena, and fluid dynamics in a swirl combustor will be discussed. The aim is not to fully explain all aspects of the fundamentals but instead to give a better background to the papers included in this thesis. Some results from the presented papers is also included in this chapter.

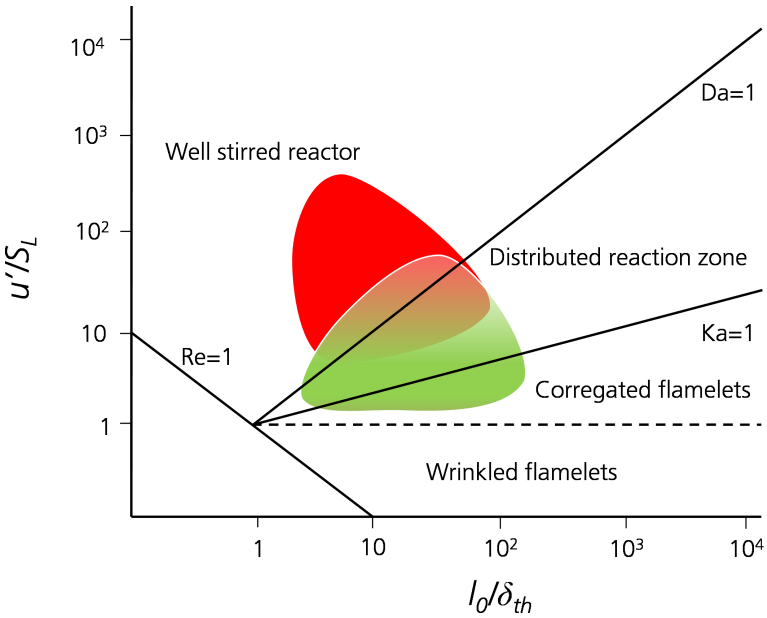

Figure 5.1: The Borghi diagram showing different flame structure regimes of premixed turbulent flames. The red area is the range for the investigated methane dominated gases and the green area is the corresponding range for the investigated syngas. The areas are approximate limits for the position in the Borghi diagram were the gases have been investigated.

5.1 The Borghi diagram

The Borghi diagram relates the turbulent and chemical scales attributed to the combustion process (Figure 5.1). The chemical scales can be extracted from one-dimensional laminar flame calculations. The chemical velocity used in the diagram is estimated by the laminar flame speed, and the chemical length scale is estimated as the flame thickness (5.1).

$$\delta_{th} = \frac{T_{in} - T_{out}}{\left(dT/dx\right)_{max}}, \tag{5.1}$$

The corresponding time scale is calculated by dividing the flame thickness by the laminar flame speed.

The turbulent scale used in Figure 26 is based on PIV measurements in paper IV [23]. The turbulent velocity is represented by the root mean square of the measured velocity fluctuations. The turbulent length scale is calculated as the integral length along a line [23,53,54]. The corresponding time scale is calculated by dividing the turbulent length scale with the turbulent velocity.

The division into different regimes by the straight lines in the Borghi diagram, is done by recognizing three dimensionless numbers. The first dimensionless number to consider is the Reynolds number. The Reynolds number relates the inertial forces to viscous forces (5.2).

$$Re = \frac{U\rho L}{\mu}, \tag{5.2}$$

In the Borghi diagram the laminar flame region is were the Reynolds number is less than unity. In order to calculate this limit certain assumptions must be made. Since the limit relates to laminar flame speed, it can be assumed that velocity (U) in Equation (5.2) equals the laminar flame speed (S_L) and the length (L) the flame thickness. If the flame thickness can be defined as the kinematic viscosity divided by the laminar flame speed (5.3), the resulting Reynolds number will be unity.

$$\delta_{th} = \frac{\mu}{\rho S_L} = \frac{\vartheta}{S_L}, \tag{5.3}$$

By using the theory of Mallard and Le Chatelier [55] the flame thickness can be estimated (5.4).

$$\delta_{th} \sim \frac{\lambda}{S_L}, \tag{5.4}$$

This approximation is done by assuming that c_p and λ are constant for the flame, and results in the thermal diffusion coefficient equalling the kinematic viscosity [55](5.5).

$$\lambda = \vartheta, \tag{5.5}$$

With these assumptions it is reasonable to expect that, below the unity Reynolds number, the flame will have laminar properties.

The second dimensionless number is the Damkhöler number (Da), which relates the turbulent time scale to the chemical time scale (5.6). At Da numbers above unity, chemistry can be assumed to dominate over turbulence and, below unity, turbulence will dominate. A unity Da is achieved when the abscissa and ordinate in Figure 5.1 are equal.

$$Da = \frac{\tau_T}{\tau_c}, \tag{5.6}$$

The third dimensionless number is the Karlovitz number (Ka) [56]. This relates the chemical time scale to the smallest turbulent time scale, i.e. the Kolmogorov time scale. When Ka is below unity, the turbulence has less influence on the flame structure. At even lower Ka, e.g. $\frac{u'}{S_L} < 1$, the flame will only be wrinkled by the fluid motion. The relationship between the abscissa and ordinate, for the Karlovitz number, (5.9) in Figure 5.1 can be derived by using the relationships (5.7) and (5.8) between the integral scales and the Kolmogorov scales.

$$\frac{\eta}{l_0} \sim \left(Re\right)^{-3/4}, \tag{5.7}$$

$$\frac{u_\eta}{u'} \sim \left(Re\right)^{-1/4}, \tag{5.8}$$

$$\frac{u'}{S_L} = \left(Ka \frac{l_0^{1/2}}{l_c}\right)^{2/3}, \tag{5.9}$$

In the Borghi diagram (Figure 5.1) the red area was the range where the methane dominated gases were investigated for the SIT burner. The green area with squares was the corresponding range for the syngas mixtures. Diluted versions of the gases down to Wobbe index $15\,\mathrm{MJ/m^3}$, equivalence ratios from 0.4 to 1.8, and pressures ranging from atmospheric to 9 bar are included in the marked areas. Some general observations was be made. Increasing the pressure moves the position north-east in the diagram. Dilution moves the position to south-west. Changing the equivalence ratio towards stoichiometry (or more accurately towards equivalence ratios with higher flame speed) moves the position to the south-east.

Changing the gas from a methane dominated gas to a syngas with high hydrogen content also moves the position to the south-east, since the syngas has higher flame speed. The burners tested range located in the Borghi diagram (Figure 5.1) assume that the turbulent velocity and the integral length scale were the same as in paper IV [23], i.e. independent of change in pressure and equivalence ratio.

5.2 Combustion chemistry

Several combustion phenomena have been discussed in the papers included in this thesis. An overview of these phenomena will be discussed under their respective chapter. Some basic chemical kinetics will also be introduced in this section. The numerical models used in the publications are excluded. Information about the perfectly stirred reactor (PSR) model, the plug flow reactor (PFR) model, and the one-dimensional laminar flame speed calculation, can be found in Chemical Reacting Flow [57] and the manual for the chemical kinetic software DARS [58]. Formation of emissions, in this case NO_X and CO, is described briefly.

In paper IX the laminar flame speed was measured and the influence of stretch was discussed. Further details about stretch are added in this chapter.

5.2.1 Emissions

The formation of emissions in gas turbine combustion follows a large matrix of chain reactions (Figure 5.2). However chemical reactions are commonly described by a global reaction. For example, the oxidation of methane can be written as a global reaction (5.10).

$$CH_4 + 2\,O_2 \longrightarrow CO_2 + 2\,H_2O, \tag{5.10}$$

This global reaction does not show the main pollutant emissions from the combustion process, e.g. CO and NO_X. These emissions are a result of a more complex chain reaction. Following the carbon reaction path (Figure 5.2), it can be seen that CO is formed before the final product CO_2. In order to calculate the amount of emissions produced during the combustion process, the full set of reactions must be known.

This is usually not the case, or the reactions may be too complex to be used in calculations. Instead, a limited range of reactions involved in the complete reaction process are usually described by a chemical kinetic mechanism. Several mechanisms for combustion of gases are described in the literature. They are usually optimized for certain fuel ranges, temperatures and pressures. The most commonly used mechanism for natural gas is the GRI 3.0 mechanism [59]. The GRI 3.0 mechanism consists of 325 elementary equations and 53 species. For syngas, a mechanism more suitable for this type of gas is recommended. One mechanism which has been used in this thesis is the San Diego mechanism [60]. The San Diego mechanism consists of 235 elementary equations and 46 species. The mechanisms contain data concerning thermodynamical properties, transport properties and chemical kinetic properties. The latter contain constants that enable the reaction rate to be calculated, using Arrhenius Law [46] (5.11).

$$k = AT^b e^{\frac{E_a}{RT}}, \tag{5.11}$$

The constants in Equation (5.11) are the pre-exponential factor A, the temperature exponent b and the activation energy E_a. There is a set of exponents for every reaction in the mechanism.

The two emission types considered in this thesis are carbon monoxide (CO) and nitric oxides (NO_X). Generally it can be said that there is an operation window for low emissions that range from the primary zone temperatures 1670 K to 1900 K (Figure 5.3) [14]. The upper temperature limit is set by the temperature dependence of NO_X and the lower limit by carbon monoxide. The increase in CO for lower temperatures is related to poor combustion and the lean blowout limit for the burner [21]. For the presented burner, the lower limit for methane might be moved towards temperatures as low as 1600 K and still keeping the CO emissions low [21]. For syngas with high hydrogen content, the limit is moved to even lower temperatures, e.g. below 1500 K. However lowering the temperature will decrease the gas turbine efficiency (Figure 2.3). The mechanisms involved in forming CO and NO_X emissions are discussed in their respective sections.

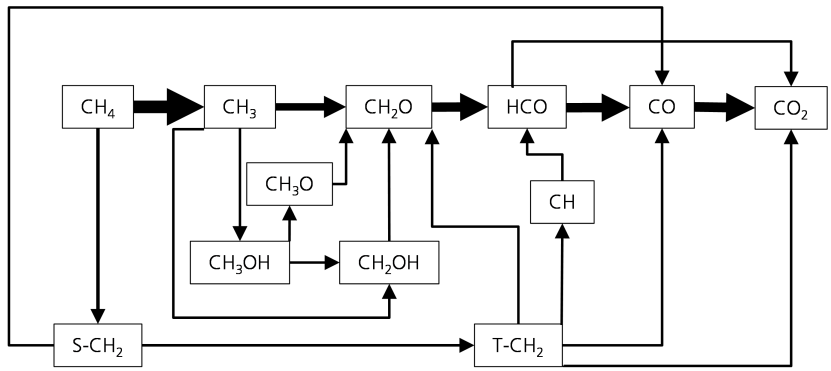

Figure 5.2: Schematic illustration of the reaction path for stoichiometric oxidation of methane to carbon dioxide. The thickness of the arrows is scaled to show the relative reaction rate. Reaction paths with less than 1 % of the maximum reaction rate are excluded. A PSR with residence time 0.15 ms using GRI 3.0 [59] as chemical kinetic mechanism is used with DARS [58].

Carbon monoxide

Carbon monoxide is a combustion species that is formed when a fuel containing carbon is oxidized. When a hydrocarbon fuel is combusted, most heat is released during the oxidation of carbon monoxide [55]. To maximize efficient usage of the fuel, this emission should be kept low. At low equivalence ratios (Figure 5.4), the carbon monoxide emissions are high, even higher than the equilibrium value for the corresponding equivalence ratio. The reason for this is that combustion is incomplete, either because there is insufficient time for the reactions to deplete CO, the premixing is poor, or the flame is quenched [14]. Increasing the equivalence ratio will lower the CO emissions until a minimum value is reached. Between this minimum and stoichiometry, the carbon monoxide emissions will increase again. This is because the combustion temperature is high enough for dissociation of carbon dioxide [14]. At rich equivalence ratios, carbon monoxide emissions will be high because there is insufficient oxygen to complete the combustion. Gas turbine combustion usually has a lean equivalence ratio, e.g. 0.6. The amount of carbon monoxide can be

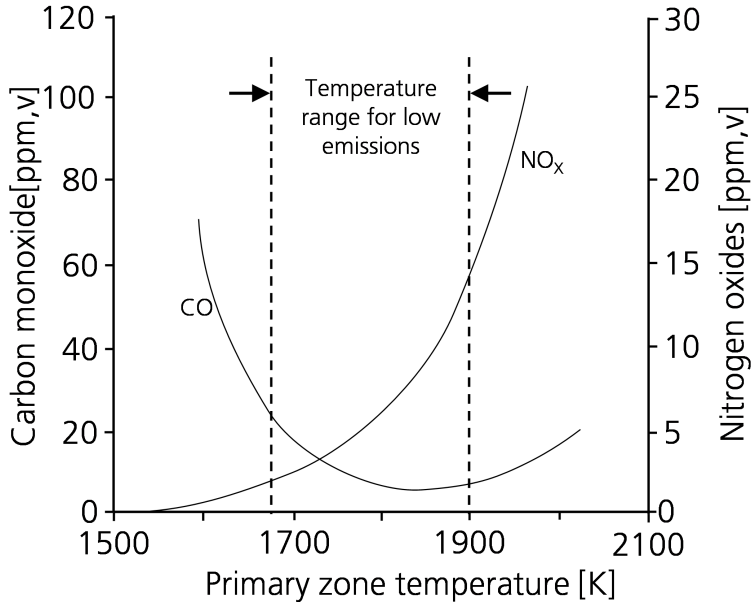

Figure 5.3: Primary zone temperature influence on NO_X and CO emissions. Adapted from Lefebvre [14].

minimized by adjusting the properties of the combustor system. A goals of such adjustments should allow longer residence times in the combustion zone, which will allow sufficient time for the carbon monoxide to approach the equilibrium value. It should also prevent poor mixing of fuel and air, which will lower the probability of pockets of partially combusted gases and prevent cooling air being injected into the combustion zone which could quench the combustion.

Nitrogen oxides

NO_X is a major pollutant that reacts to form smog and acid rain, and can form ozone in the troposphere. Keeping NO_X at a minimum is important both for health reasons and environmental reasons. Legislation is driving combustion processes towards lower NO_X levels [61]. In

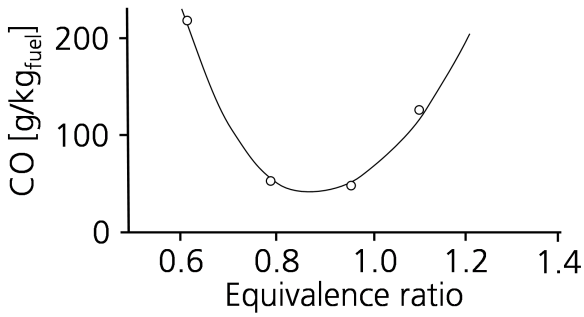

Figure 5.4: Influence of equivalence ratio on CO emissions at atmospheric conditions. Adapted from Lefebvre [14].

conventional gas turbines the primary reason for NO_X formation is high temperatures, namely thermal NO_X [5]. Furthermore, conventional gas turbine combustors operate in diffusion mode or with limited mixedness. This causes the flame to burn at higher temperatures, which increases the production of thermal NO_X. The most important reactions included in thermal NO_X or as it is also called the Zeldovich mechanism are [55,62]:

$$O + N_2 \rightleftharpoons NO + N, \tag{5.12}$$

$$N + O_2 \rightleftharpoons NO + O, \tag{5.13}$$

$$N + OH \rightleftharpoons NO + H, \tag{5.14}$$

The rate limiting step is the first one (5.12). The presence of thermal NO_X is emphasized at temperatures above 1850 K [14].

Another reaction path for NO_X production is Prompt NO_X [63]. The two foremost reactions involved in prompt NO_X are [4]:

$$CH + N_2 \rightleftharpoons HCN + N, \tag{5.15}$$

$$C + N_2 \rightleftharpoons CN + N, \tag{5.16}$$

NO is then on formed for example via the reaction (5.17).

$$N + OH \rightleftharpoons NO + H, \tag{5.17}$$

Table 5.1: Reaction pathways for nitrogen [22]

Gases	Equivalence ratio	Reaction flow % Nitrous Oxide	NNH	Prompt	Thermal
Methane	0.47	53.7	29	7.2	10.1
	1.21	-1.3	3.3	54.8	43.2
	1.40	0	-1.0	67.4	38.66
Syngas	0.45	39.5	52.5	1.3	6.7
	1.05	5.3	14.1	6.4	74.2
	1.40	0.0	17.3	32.4	50.3
Diluted	0.48	36.2	55.5	1.6	6.7
Syngas	1.05	4.7	25.6	10.4	59.3
	1.40	9.9	20.9	30.2	39.0

The Prompt pathway increases in importance when increasing the equivalence ratio from 0.6 to 1.4 (Table 5.1). It should be noted that even if the forward path of Prompt NO_X is increased here, the reaction pathways within the Prompt NO_X mechanism can, in some cases, decreases NO_X emissions [4,64]. A simple PSR reactor test shows that this decrease of NO_X emissions increases with pressure [31]. Myerson [65] also shows how the HCN pathway might be used to reduce NO by addition of hydrocarbon and oxygen to the combustion exhaust gases. The Fenimore mechanism has less impact on syngas, with limited hydrocarbon content, as investigated in this thesis, since this mechanism is attributed to hydrocarbon combustion.

At lean combustion a pathway via nitrous oxide (N_2O) prevails. The reactions that participate in this reaction path are [4]:

$$O + N_2 + M \rightleftharpoons N_2O + M, \tag{5.18}$$

$$H + N_2O \rightleftharpoons NO + NH, \tag{5.19}$$

$$O + N_2O \rightleftharpoons NO + NO, \tag{5.20}$$

For syngas mixtures, in particular, the path via dinitric hydride (NNH) [22,66] becomes important at lean combustion. The two most significant

reactions for the NNH intermediate route are [66]:

$$NNH \rightleftharpoons N_2 + H, \tag{5.21}$$

$$NNH + M \rightleftharpoons N_2 + H + M, \tag{5.22}$$

NO is then formed via reaction (5.23):

$$NNH + O \rightleftharpoons NH + NO, \tag{5.23}$$

Figure 5.5 show the complexity of NO_X formation using GRI 3.0 as chemical kinetic mechanism for methane combustion. In Table 5.1, it can be seen that for the investigated equivalence ratio the nitrous oxide path is the most prominent at leaner mixtures.

Fuel-bound nitrogen path is not discussed in this thesis, as no nitrogen was bound in the fuels investigated.

Nitrogen oxides - selected results

NO_X emissions for the presented burner could be optimized by varying the equivalence ratios of the individual burner sections [22]. For example running the RPL at leaner equivalence ratios lowers the total NO_X levels. For methane, the highest NO_X emission is found at RPL equivalence ratio 1.6. Intuitively the highest NO_X emission should be were at the equivalence ratio where the temperature is the highest, i.e. approximately at stoichiometry. The most plausible explanation why the highest NO_X emission does not occur at stoichiometric RPL equivlence ratio, is because of incomplete incomplete combustion inside the RPL and the subsequent diffusion flame-like combustion after the RPL. For syngas the peak NO_X emission agreeing with the highest adiabatic flame temperature [22], i.e. close to stoichiometry, although there is a slight shift towards a higher equivalence ratio (Figure 5.6).

The investigation of the fuel partitioning between the Main and the Pilot in paper VII [22], shows that minimizing the amount of fuel to the Pilot minimizes NO_X emissions (Figure 5.7). CFD calculations by A.

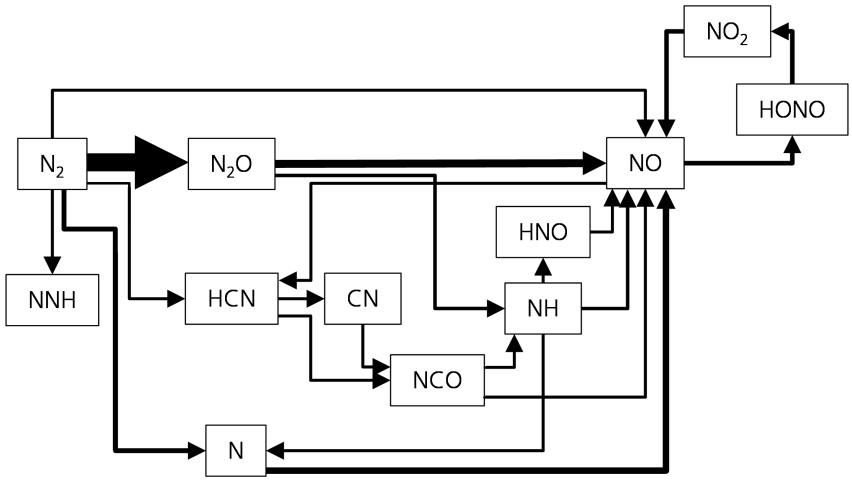

Figure 5.5: Schematic illustration of the reaction path for oxidation of nitrogen to nitrogen oxide for methane at equivalence ratio 0.6. The thickness of the arrows is scaled to show the relative reaction rate. Reaction paths with less than 5 % of the maximum reaction rate are excluded. A PSR with residence time 0.5 ms using GRI 3.0 [59] as chemical kinetic mechanism is used with DARS [58].

Abou–Taouk [31,42] was used to indicate that the Pilot was incompletely premixed in the combustion zone. The unmixedness of the Pilot is the most likely explanation why minimizing the fuel to the Pilot section minimizes NO_X emissions. If both the Main and the Pilot section had been perfectly premixed, the minimum NO_X emission should have been where the equivalence ratio of the Pilot and the Main was the same. This would limit the existence of higher (than mean) equivalence ratios originating from either of the two burner sections, which would otherwise increase the temperature dependent NO_X production.

The pressure influence on NO_X emission from the burner was investigated in paper VII [31]. The main conclusion of this investigation is that, for combustion involving high temperature regions, as for the presented burner, there will not be a strict pressure influence, instead the NO_X

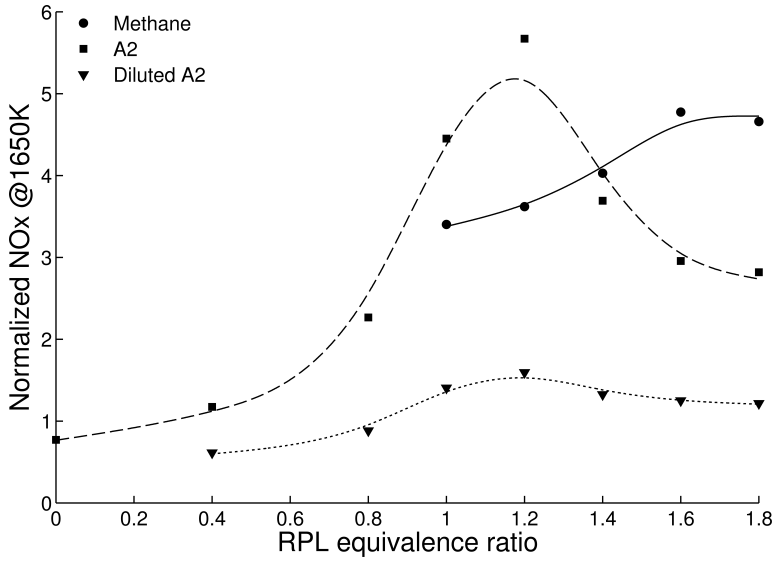

Figure 5.6: NO_X emissions for varying RPL equivalence ratios [22].

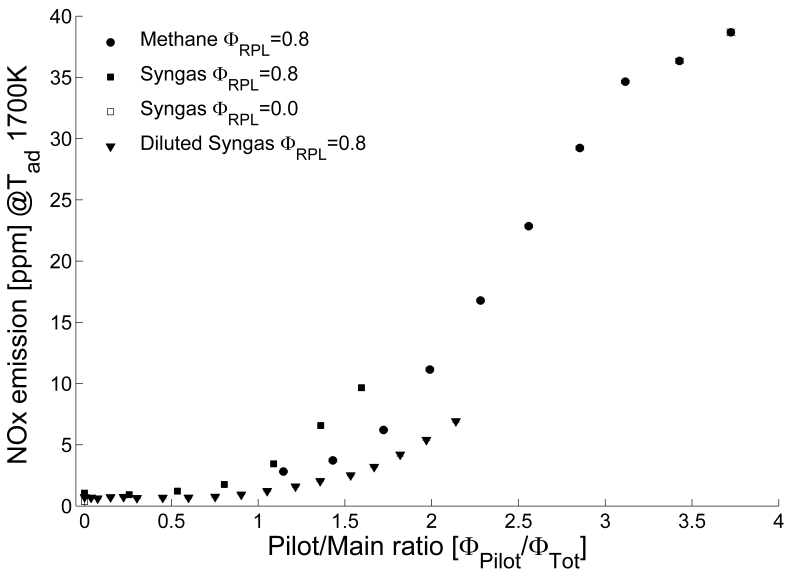

Figure 5.7: NO_X emissions with varying fuel partitioning [22].

production follows the theory of thermal NO_X (Figure 5.8). However, for rich combustion there can be an inverted pressure dependence due to the decrease of NO_X emissions with increasing pressure, caused by the HCN radical [4,31,64,65]. A decrease in NO_X emissions with pressure has also been observed by Matuszewski and Jansohn [67], in a combustor with flue gas recirculation.

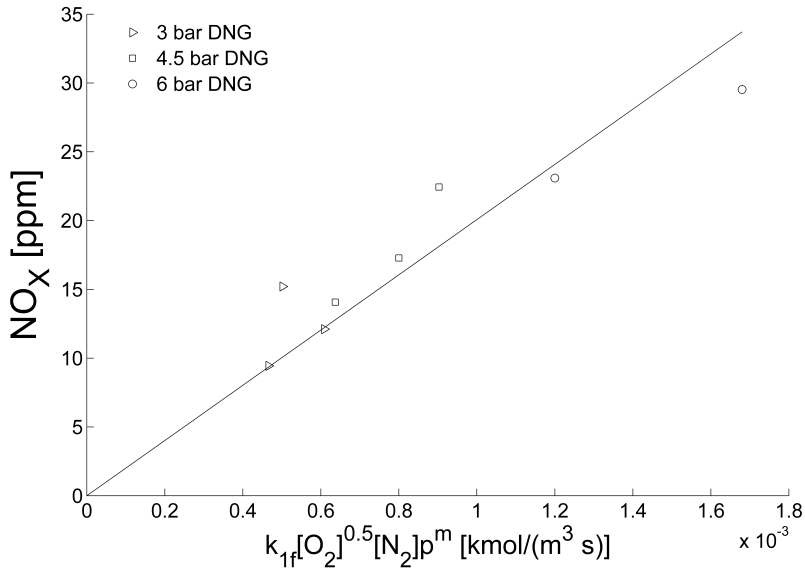

Figure 5.8: NO_X concentration for the full burner plotted against the rate of formation, m=0 [31].

5.3 Chemistry and fluid dynamics coupled phenomena

In most combustion cases, there is a coupling between chemistry and fluid dynamics. In the two sections, stretch and lean blowout (LBO) will be discussed. Both of these phenomena are affected by the coupling between chemistry and aerodynamics.

5.3.1 Flame stretch (applied on a laminar conical flame)

The laminar flame speed can be defined as the speed of the unburned gas relative to the flame front in a freely propagating flame with zero stretch. In paper IX [30], the flame speed was measured for a conical flame. A conical laminar flame, like the one from a Bunsen burner, has a curved surface. This curved surface together with the downstream velocity profile, i.e. the velocity gradient, will influence the flame properties. This influence is known as flame stretch. Flame stretch is quantified by the normalized local time derivative of the flame surface [45,56,68]. This is called the stretch rate (5.24).

$$\kappa = \frac{1}{A}\frac{dA}{dt}, \tag{5.24}$$

The effect that stretch has on the flame depends on diffusion. Most pronounced is the relationship between the thermal diffusion and the diffusion on the deficient reactant [8].

Assuming that the conical flame is approached by a constant velocity profile, the stretch will be negative. The negative stretch is caused by the curved surface of the flame. Since the flame is moving towards the fresh gas mixture, the flame area will become smaller, causing the negative stretch. The stretch due to the curvature in the conical flame causes heat to diffuse into the smaller area of the unburned gas mixture, increasing the temperature of the unburned mixture. This increases the flame speed. In contrast, the limiting reactant in the fresh gas mixture will diffuse outward into a larger area, thereby lowering the intensity of combustion [8]. The preferential diffusion between heat and the limiting reactant is characterized by the Lewis number (5.25).

$$Le = \frac{\lambda}{D_L}, \tag{5.25}$$

At unity Lewis number, the relation between thermal diffusivity and the limiting reactant diffusivity cancel each other out and there will be limited effect of stretch [8]. At Le$>$1, the thermal diffusivity will be prominent and the flame speed will increase. For Le$<$1 the diffusivity of the limiting reactant will prevail and the flame speed will be lower. The relationship between the diffusivity of the limiting reactant and the

excess reactant also affects the flame, but to a lesser extent than the Lewis number [8].

Traditionally when measuring the laminar flame speed from a conical flame, rotational symmetry of the flame and top-hat velocity profile is assumed. The flame speed can then be calculated either by the bulk volume flow, prior to combustion, divided by the total area of the flame, or by calculating the half-angle of the flame and project the upstream velocity on the normal of the flame. Both of these methods can be corrected to take into account the negative stretch effect of the Bunsen burner. The correlations usually involve using Lewis number and Markstein length or linear extrapolation to zero stretch [69,70]. In reality it is hard to achieve a top-hat velocity profile out of a tube. In paper IX [30], the velocity profile was measured using PIV. The velocity profile was clearly not a top-hat profile (Figure 5.9).

To be able to calculate the flame speed with the half-angle method, it should be calculated at the shoulder region of the flame where the half-angle can be considered constant with radius. However, since the velocity profile was not a top-hat profile, the calculated local flame speed could vary with as much as 20 % depending on the flame position on which the calculation is based. This variation is likely caused by stretch. Realizing that the velocity gradient has a positive effect on stretch, a radial position can be found at which the stretch effects on the flame is negligible (Figure 5.10). This is the basis of the methodology for calculating the stretch-free laminar flame speed in paper IX [30].

The presented methodology eliminates the need for stretch correlation. The methodology uses the analytical stretch formulation based on the derivation of flame stretch for a conical flame [69] (5.26).

$$\kappa = -\left[\frac{\sin\alpha}{r}\frac{\partial}{\partial r}\left(ru\cos\alpha\right) + \cos\alpha\frac{\partial}{\partial z}\left(u\cos\alpha\right)\right], \tag{5.26}$$

The second derivative is neglected, by assuming that there is negligible change in velocity and flame angle in the axial direction. The resulting equation can be further simplified by assuming that there is insignificant change in flame angle with radius (5.27). This is true in the shoulder

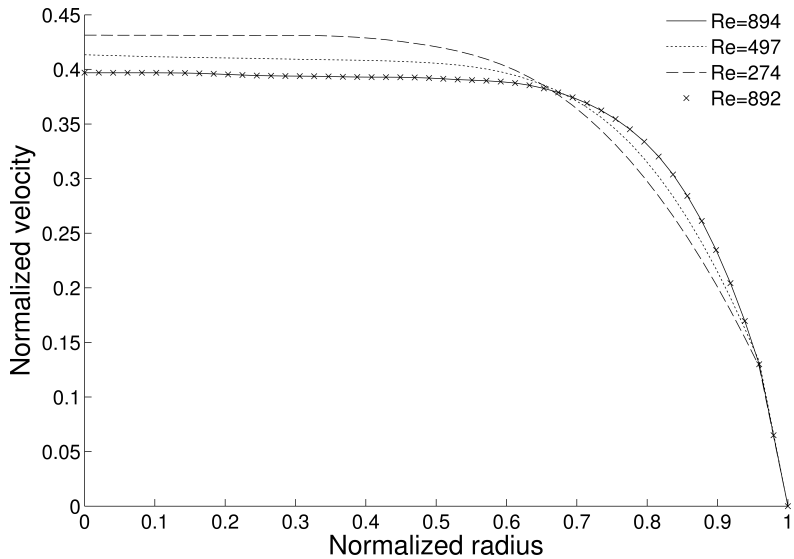

Figure 5.9: The normalized velocity profiles for the 10 mm nozzle. The marker (x) shows an interpolated flow profile for Re=892, which corresponds to the methane measurements at equivalence ratio 1.056 in paper IX [30].

region.

$$\kappa = -\frac{\sin\alpha}{r}\left[r\cos\alpha\frac{\partial u}{\partial r} + u\cos\alpha\right], \tag{5.27}$$

In Equation (5.27), the left part inside the brackets is the stretch effect caused by the velocity gradient and the right part is due to the curvature of the flame. Since the velocity gradient is negative it counteracts the effect of flame curvature. Figure 5.11 shows how the stretch correlated laminar flame speed from paper IX compares to the unstretched method, numerical models and previous measurements [30].

The presented methodology for excluding the stretch effect from the laminar flame speed measurement has some limitations. Firstly, the zero stretch position has to be in the within the shoulder region where the

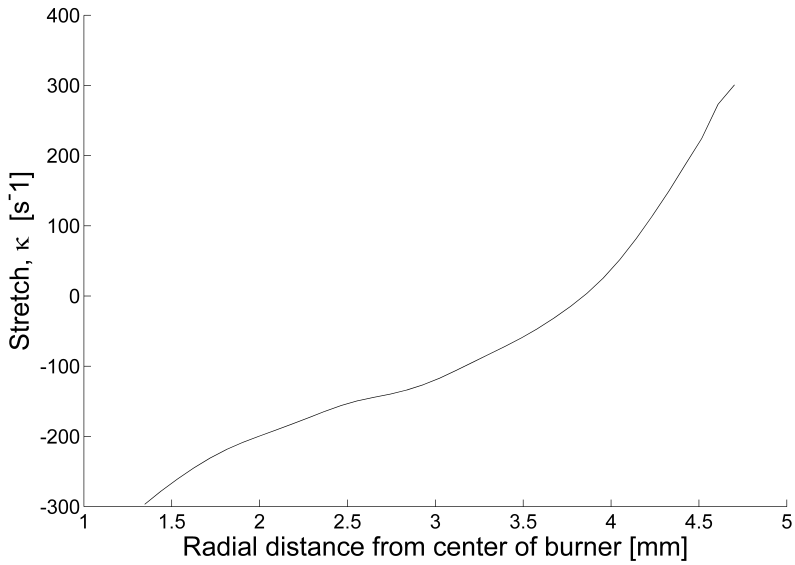

Figure 5.10: Variation of stretch with radius. Computed from the measurements of methane at equivalence ratio 1.056, at room temperature, from paper IX [30].

flame angle is not a function of radius. This position also has to be sufficiently far away from the stabilizing burner rim to avoid loss of heat and radicals. Furthermore, the calculated stretch free laminar flame speed is sensitive to the zero stretch location with regard to the velocity profile. As an example, the sensitivity of the flame speed to radial position of zero stretch is calculated for Figure 5.10, $\frac{dS_L}{dr_0} \approx 0.09\,\mathrm{m/(s\,mm)}$, and the sensitivity of the flame speed to the velocity profile change with regards to Reynolds number, $\frac{dS_L}{dRe} \approx 3.2{\times}10^{-5}\mathrm{m/s}$. This implies that, an error in zero stretch radial position of ≈5 %, e.g. 0.2 mm, gives an error in laminar flame velocity of 4.5 %, and an error in Reynolds number of ≈5 %, e.g. ΔRe=45, gives an error in laminar flame velocity of 0.14 %.

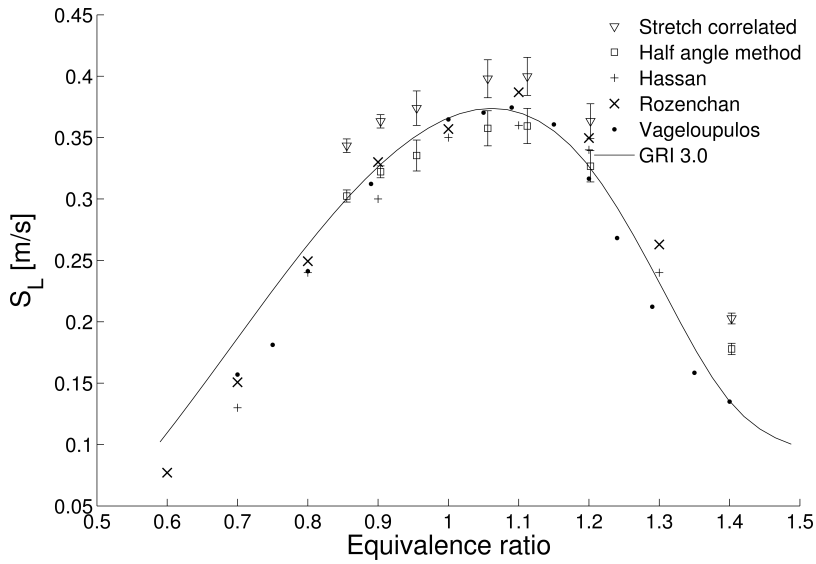

Figure 5.11: Stretch correlated laminar flame speed measurements together with the half angle method based laminar flame speed for the same data [30]. The data is validated against previous measurements [71-73] and compared to the numerical results from the GRI 3.0 mechanism [59].

5.3.2 Lean blowout

Blowout is the phenomena when a flame is lifted or extinguished by being pushed downstream of the intended flame position. Moving the lean blowout limit towards lower values is important for limiting NO_X emissions while ensuring stable and complete combustion. There are different theories on what causes a flame to blowout. Normally, three different theories that affect the height of lift off, which is a sign of blowout, are mentioned [4]. The first theory says that if local flame speed is lower than the approaching fluid velocity the flame will move downstream, i.e. $u > S_T$. The second theory deals with the case when the local strain rate in the fluid exceeds the extinction strain rate [74,75], i.e. $\epsilon > \epsilon_{cr}$. This will cause the flame to locally extinguish, which lowers the flame temperature and subsequently the flame speed. The third theory considers the back mixing by large-scale flow structures that supply hot product gases to the

fresh mixtures, causing them to heat up and the flame speed is increased [68,76]. If the mixing time of the large scale structures is shorter than the chemical time, i.e. $\tau_l > \tau_{ch,cr}$, there is not enough time available for the fresh mixture to be ignited by the hot mixtures. As consequence, this the flame temperature locally and the flame speed is decreased. In addition to these theories, fuel composition has a profound influence on the flame speed and on the blowout limit. It has been shown that fuel compositions with high hydrogen content have a lower lean blowout equivalence ratio [21,73,77-80]. LBO investigations where the swirl strength is varied have shown that swirl has influence on the LBO limit [79,81]. Furthermore, other factors like physical mixing and operating conditions, e.g., pressure, temperature, may exert an influence .

In this thesis, the lean blowout limit was examined by varying the equivalence ratio in the RPL [21]. It could be seen that an increase in RPL equivalence ratio decreased the lean blowout limit (Figures 5.12 and 5.13). This effect was most pronounced for the syngas (Figure 5.12).

Increasing the equivalence ratio in the RPL will increase the available energy that stabilizes the combustion of the burner. Since lean blowout occurs at sub-unity equivalence ratios, RPL equivalence ratios higher than the equivalence ratio in the outer burner sections will, at least locally, increase the flame equivalence ratio outside the RPL towards stoichiometry [82]. The increase in available energy together with the increase of equivalence ratio towards stoichiometry could explain why an increase in RPL equivalence ratio decreases the lean blowout limit of the burner.

In paper III [32] it was shown that a rich RPL creates a second combustion zone for the RPL exhaust gases as they are mixed with surrounding air. The OH–signal for methane (Figure 5.14) shows that the second combustion zone becomes weaker at equivalence ratio 1.8. This is also where the positive effect of increasing the RPL equivalence ratio is diminished (Figure 5.13).

The influence that a pre-chamber combustor (like the RPL) has on the LBO limit was qualitatively modelled in paper I by using two PSR reactors in series [82]. When increasing the equivalence ratio of the pre-

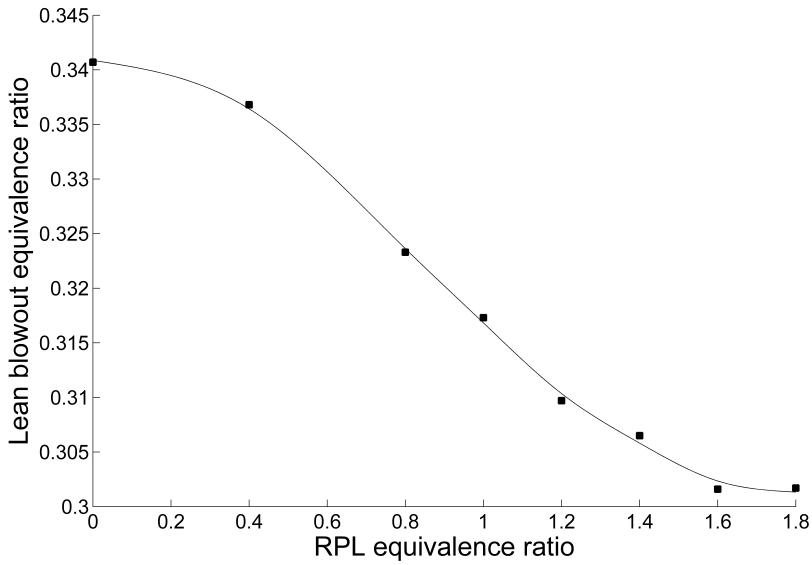

Figure 5.12: Change in lean blowout limit for syngas when varying RPL equivalence ratio [21].

chamber (the first PSR), the tendency was similar that shown by the measurements in Figures 5.12 and 5.13, i.e. increasing the equivalence ratio of the pre-chamber extends the lean blowout limit (Figure 5.15). The reason for this is, again, that the combined mixed equivalence ratio in the second PSR is being moved towards stoichiometry, which in turn increases the temperature.

In addition to the temperature effect, for lean methane and syngas it can be seen that lowering the residence time in the first PSR extends the lean blowout limit. This contradicts the temperature effect (Figure 5.16). It was indicated in paper I [82] that the reason for this is the increase of the radicals O, H and OH, originating from the first PSR reactor. The importance of the radicals O, H and OH, is well described in literature. It has been shown that these radicals have great influence on the sensitivity for laminar flame speed calculations [45], and are important in the

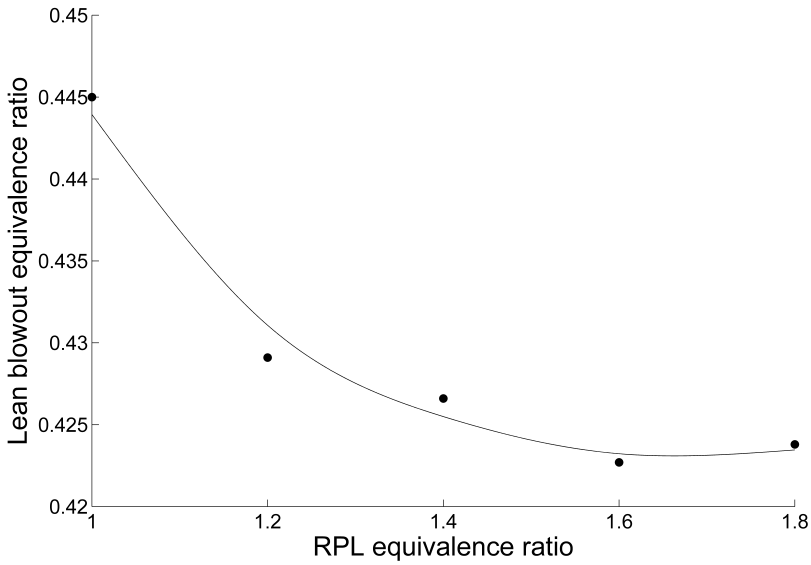

Figure 5.13: Change in lean blowout limit for methane when varying RPL equivalence ratio [21].

oxidation process of methane, hydrogen and carbon monoxide as they contribute strongly to the chain branching process [4,46].

Traditionally, blowout is characterized by an operating envelope where the fuel air ratio is a function of the mass flow [14]. Figure 5.17 shows that the range of equivalence ratios becomes smaller for increasing mass flow and decreasing pressure. For syngas, the limit of the operating range is not only limited by blowout. Since syngas has a high hydrogen contents, it is prone to flashback, i.e. the flame moves upstream from the intended flame zone. This may cause damage to the burner and materials that the flame might attached to. In this thesis flashback was observed [21]. The flashback caused the flame to become attached to the RPL rim.

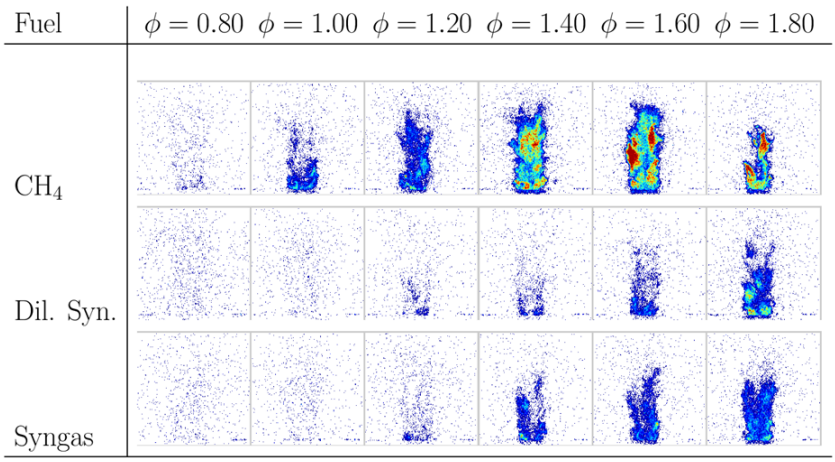

Figure 5.14: Single pulse OH-LIF images for varying equivalence ratios and fuel. Colour bar is uniform for all images and ranges from 0 to 400 counts, blue to red. All images are background subtracted, but there is no correction for laser sheet inhomogeneity [32,82].

5.4 Fluid dynamics in a swirl combustor

In a gas turbine, fluid dynamics affect many different parts of the combustor. For example, the fluid dynamic influence is already relevant before the combustion zone. Specifically for premixed low NO_X combustion, where it is of the utmost importance to achieve sufficient premixing [22,82]. If the flow is not mixed properly it is difficult to achieve low NO_X emissions. In the flame zone, stable combustion is achieved through fluid dynamics, usually either by a bluff body [16,74,76] or a swirling flow [17,23,26].

The swirling motion creates a recirculation zone that transports hot combustion gases back to the combustion zone (Figure 5.18) [23]. The hot gases stabilize the combustion by supplying heat and reactive radicals to the flame zone. Using PIV as diagnostic method, no major change could be found in the recirculated mass flow, comparing the different combustion gases [23]. (An exception to this was the diluted syngas

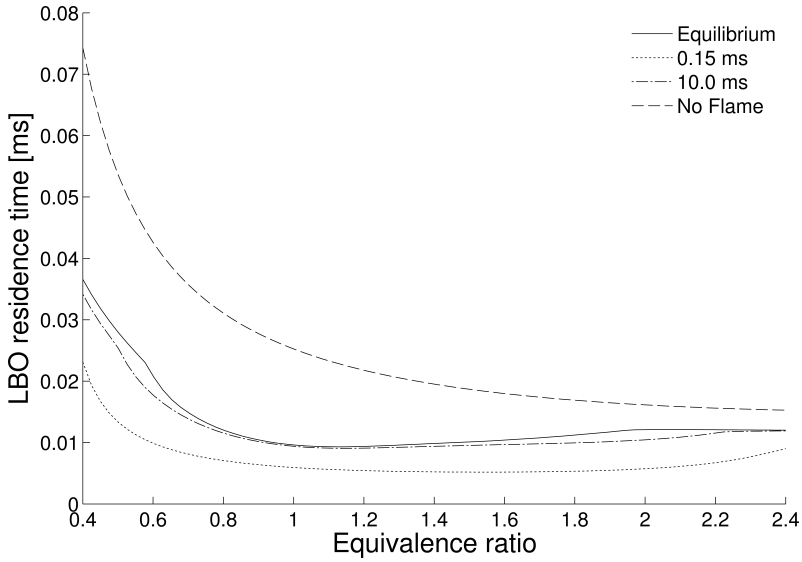

Figure 5.15: The LBO residence times for the second PSR vs equivalence ratio in the first PSR for syngas [82].

where two out of three measured recirculation zones were shorter than all other recirculation zones (Figure 5.18). The explanation for this is yet to be found.) Syred, Chigier and Beér [26] also found, that under strong recirculating conditions there was little change in recirculation zone size between different combustion cases. In general it can be said that the swirl number should be >0.6 to achieve a strong recirculation [17].

Besides swirl, the turbulence in the combustion zone has a strong influence on how fast the flame will propagate. A review by Driscoll [83] stipulates that the turbulent flame speed is a function of the reaction layer surface area per unit volume, the flame brush thickness, and the stretch factor (5.28).

$$\frac{S_T}{S_{L0}} = I_0 \Sigma_{max} \delta_T, \tag{5.28}$$

Turbulence affects the flame both by wrinkling the flame [84] and by broadening the flame front [83]. Flame wrinkling is affected by the large

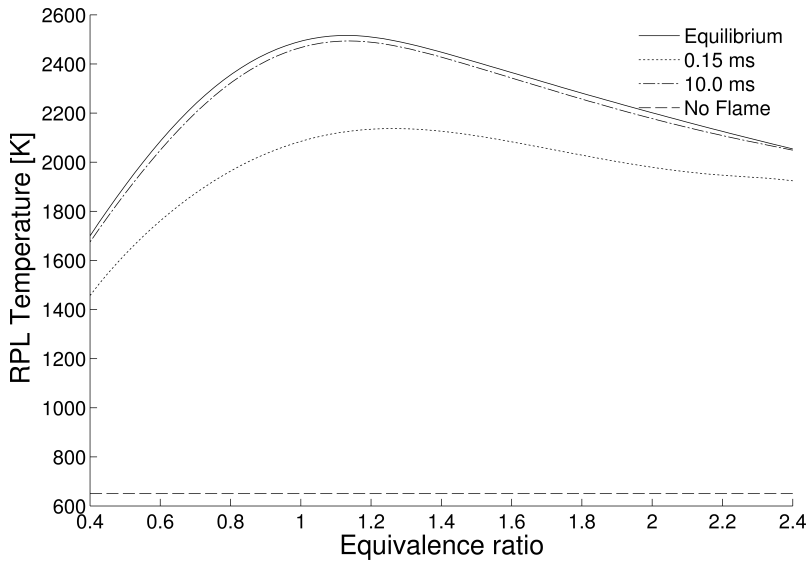

Figure 5.16: The reactor temperatures in the first PSR vs equivalence ratio in the first PSR for syngas [82].

scale motion of the fluid, while flame broadening is generated by small scale motion [84]. Turbulent flow contains a cascade of scales ranging from larger scales down to smaller scales. The turbulence is sustained by the energy from the bulk flow which creates the large scale motion by interaction with the channel geometry. These large scale motions can be visualized in the flow as rotating eddies (Figure 5.19). The large scale eddies are broken down to smaller eddies which in the end gets dissipated by viscous stresses [53,54,85].

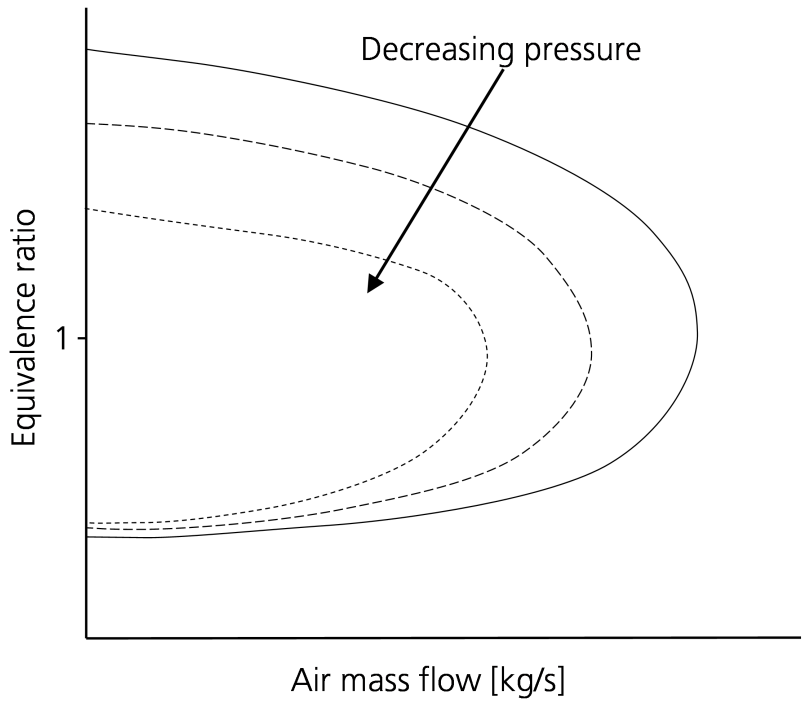

Figure 5.17: Stability range for typical gas turbine combustors for varying mass flow, equivalence ratio and pressure. The stable region is inside the loops. Adapted from Lefebvre [14].

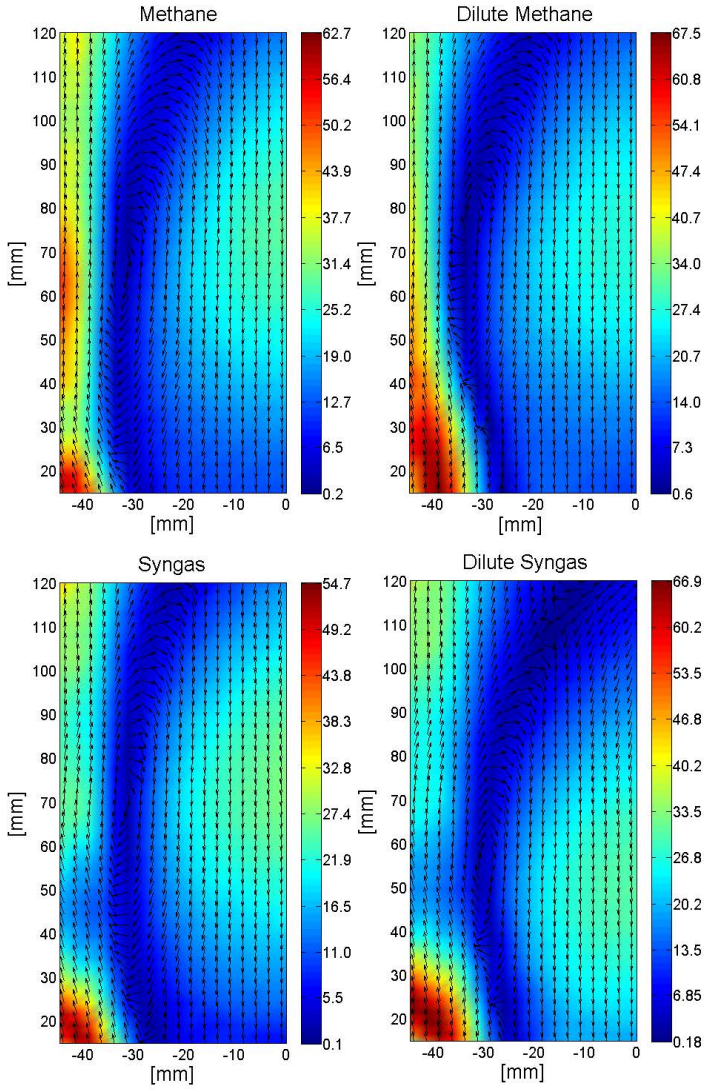

Figure 5.18: Mean velocity fields from PIV measurements for four combustion gases. The colour bars show the absolute velocity in m/s. The velocity vectors are normalized by their individual absolute velocity and only show the direction of the flow [23].

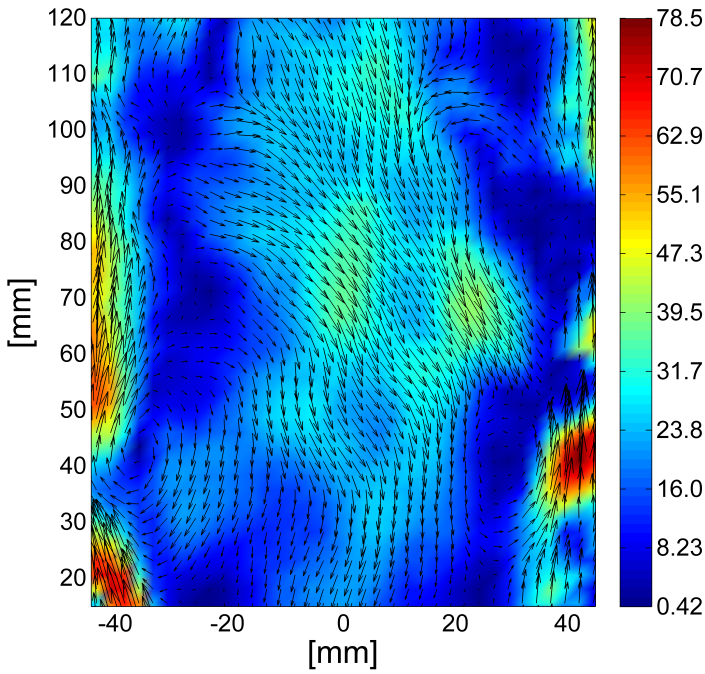

Figure 5.19: Single shot PIV image showing the recirculation zone with counter-rotating eddies. The colour bar show velocities in m/s. The image originates from the data set produced in paper IV [23].

CHAPTER 6

Concluding remarks

This thesis has presented experimental results from four different setups: one laminar flame speed setup and three setups that investigated a downscaled version of an industrial burner part of the SGT-750 gas turbine. The main measurement techniques used were emission probing (e.g. measurements of CO and NO_X), PIV, OH-LIF and Schlieren imaging. The experiments were conducted under both atmospheric and pressurized conditions, at a preheat temperature of 650 K.

The laminar flame speed measurements were used to validate chemical kinetic mechanisms. Specifically, it was found that the GRI 3.0 mechanism was preferred for gases that are based on methane and the San Diego mechanism was more suitable for the syngas mixtures.

The main conclusions from the atmospheric investigation of the the experimental burner were:

- The lean blowout limit could be extended by increasing the RPL equivalence ratio.

- The lean blowout equivalence ratio was significantly lower for the syngas than the methane based gases.

- The lean blowout was affected both by the heat supplied from the RPL and the reactive radicals O, H and OH.
- NO_X emissions could be minimized by lowering the equivalence ratio in the RPL and Pilot burner sections.
- NO_X emissions originated from burner sections where the mixedness was limited.
- Single digit NO_X emissions were achievable at atmospheric pressure.
- The emission measurements, OH-LIF and PIV could be used to validate CFD calculations.
- Comparisons of the POD modes from PIV measurements and CFD calculations could be used to validate dynamical phenomena for the CFD calculations.
- Combustion of diluted gases down to Wobbe index $15\,MJ/m^3$ was achievable.

The main conclusions from the pressurized investigation of the experimental burner were:

- Ignition of the RPL was possible at pressures up to 9 bar and dilutions down to Wobbe index $15\,MJ/m^3$.
- Increasing the pressure does not appear to drastically change the flame location inside the RPL, neither does it drastically change the structure of the OH distribution outside the RPL.
- The pressure influence on NO_X emissions for the burner agree with the Zeldovich mechanism.
- The presence of HCN radical reduces the NO_X emission with increased pressure.

As this project has a continuation, I would like to mention a couple of areas that could be the focus of future investigations. One area is why the PIV measurements for the dilute syngas have two different sizes on the

recirculation zone for the same settings; One that correspond with the recirculation zones of the other combustion cases while a second recirculation zone is situated closer to the position of the non combustion case. This recirculation zone also has a higher fluctuating velocity, which could indicate instabilities that cause the recirculation zone to shift position.

The influence of a Quarl increases the positive effects of the recirculation zone. It could be of interest to find out what the optimal Quarl angle is in comparison to swirl number for stabilization and NO_X emissions. Furthermore, combustion with and without the Quarl could be compared.

As the present work was limited in its field of view access due to the Quarl, it would be interesting to see if the interaction of the different burner sections could be visualized with both OH-LIF and PIV. This could be done both by removing the Quarl and replacing the steel Quarl with a quartz Quarl.

CHAPTER 7

Summary of publications

Paper I:

Radicals influence on the lean blowout limit for an industrial DLE gas turbine burner

By: **Ivan R. Sigfrid**, Ronald Whiddon, Robert Collin and Jens Klingmann

Submitted to Combustion and Flame: CNF-D-13-00243

This paper investigates the influence of combustion intermediates on the lean blowout limit. A network of two perfectly stirred reactor models in series was used to simulate the lean blowout. In addition laser-induced fluorescence was used to qualitatively show the existence of the OH radical in the re-ignition zone. Experimental data for lean blowout was used as comparison for both the reactor network simulations and the OH-LIF.

My contribution to this paper was to create the reactor network and perform the network simulations. I also conducted the analysis of the network investigation. The OH-LIF experimental work, post-processing

and analysis were performed by R. Whiddon. R. Collin supervised the OH-LIF experiments. I wrote the paper, as the lead author. The OH-LIF part was written by R. Whiddon and R. Collin. R. Collin and J. Klingmann supervised the writing.

Paper II:

Experimental and Reactor Network Study of Nitrogen Dilution effects on NO_X Formation for Natural Gas and Syngas at Elevated Pressures

By: **Ivan R. Sigfrid**, Ronald Whiddon, Robert Collin and Jens Klingmann

ASME Turbo Expo 2013: GT2013-94355

This paper is an investigation of NO_X formation in a prototype fourth generation DLE burner. The investigation was performed at the high pressure combustion facility at Lund University. The gases tested were natural gas, methane and syngas. Diluted versions of the gases were also tested. The pressures tested ranged from 3 bar to 9 bar. The experimental test results were modelled using a PSR/PFR network to gain insight into the complex NO_X chemistry.

My contribution to this paper was planning and construction of the experimental setups, including a new high pressure fuel gas mixing station. I also led the initiative of reconstructing the high pressure facility to enable housing of the experimental burner. I planned the test schemes (fuel and air, flows, temperatures and pressures) in cooperation with SIT via the Turbo Power group, "Comb 2", and Rutger Lorensson. I led the experimental work. The OH-LIF experimental work, including post-processing and analysis thereof, were performed by R. Whiddon. R. Collin supervised the OH-LIF experiments and conducted some of the measurements. I was lead author, and wrote the paper and conducted the reactor network analysis. R. Collin and J. Klingmann supervised the writing.

Paper III:

Investigation of a Premixed Gas Turbine Combustor Central Body Burner using OH Planar Laser Induced Fluorescence at Elevated Pressures

By: Ronald Whiddon, **Ivan R. Sigfrid**, Robert Collin, Jens Klingmann, Marcus Aldén

ASME Turbo Expo 2013: GT2013-94443

This paper is an OH-LIF investigation of the central body burner (RPL) of a prototype fourth generation DLE burner. The investigation was performed at the high pressure combustion facility at Lund University. The gases tested were methane and syngas. Diluted versions of the gases were also tested. The pressures tested ranged from 3 bar to 9 bar. The post RPL combustion was investigated, showing how the OH-signal, as a marker for the flame structure, changed with equivalence ratio, gas and pressure. The flame structure was compared to the flame position inside the RPL, based on RPL wall temperature measurements.

My contribution to this paper was, besides the planning of the experiment as in Paper I, was to interpret the experimental results and assist R. Whiddon as co-writer. R. Whiddon conducted the OH-LIF post-processing and was the lead author. R. Collin supervised the OH-LIF experiments. Marcus Aldén supervised R. Collin, Marcus Aldén and J. Klingmann supervised the writing.

Paper IV:

Experimental Investigation of an Industrial Lean Premixed Gas Turbine Combustor with High Swirling Flow

By: **Ivan R. Sigfrid**, Ronald Whiddon, Abdallah Abou-Taouk, Robert Collin, Jens Klingmann

ASME 2012 Gas Turbine India Conference: GTIndia2012-9681

In this paper, PIV and OH-LIF measurements were conducted in an atmospheric setup with a prototype fourth generation DLE burner. The results are used to discuss the effect of varying fuel gas composition on combustion and fluid mechanical properties, e.g. recirculation zone and velocity fluctuations. Relevant time and length scales are also derived. The PIV measurements and OH-LIF measurements are compared to CFD simulations.

My contribution, besides being the lead author, was choosing the test scheme settings, setting up and performing PIV measurements, deriving and calculating scale properties, and evaluating the results. R. Whiddon performed the OH-LIF measurements and post-processing thereof. A. Abou-Taouk performed the CFD simulations and supplied the CFD results. R. Collin and J. Klingmann supervised the writing.

Paper V:

A Four-Step Global Reaction Mechanism for CFD Simulations of Flexi-Fuel Burner for Gas Turbines

By: Abdallah Abou-Taouk, **Ivan R. Sigfrid**, Ronald Whiddon, Lars-Erik Eriksson

Turbulence, Heat and Mass Transfer 7

In this paper, a four-step global mechanism was optimized for syngas combustion. The mechanism was used in CFD modelling of a prototype fourth generation DLE burner. The CFD results were compared with PIV images, OH-LIF and POD analysis.

My contribution was choosing the test scheme settings, setting up and performing PIV measurements, deriving and calculating scale properties (for PIV and CFD), and performing the POD analysis (for PIV and CFD). A. Abou-Taouk was the lead author and performed the CFD calculations and validation thereof. R. Whiddon was in charge of the OH-LIF measurements. L. E. Eriksson supervised the writing.

Paper VI:

CFD Investigation of Swirl-Stabilized Flexi-Fuel Burner Using Methane-Air Mixture for Gas Turbines

By: Abdallah Abou-Taouk, **Ivan R. Sigfrid**, Ronald Whiddon, Lars-Erik Eriksson

ISABE 2011: ISABE-2011-1122

In this paper, a multi-step global mechanism is applied to CFD analyses of a prototype fourth generation DLE burner. The results are compared with PIV, OH-LIF data and emissions data.

My contribution was choosing the test scheme settings, setting up the emission system and performing the PIV measurement. A. Abou-Taouk performed the CFD simulations and optimization thereof. R. Whiddon performed the OH-LIF measurements. L. E. Eriksson supervised the writing.

Paper VII:

Parametric Study of Emissions from Low Calorific Syngas Combustion, with Variation of Fuel Distribution, in a Prototype Three Sector Burner

By: **Ivan R. Sigfrid**, Ronald Whiddon, Marcus Aldén, Jens Klingmann

ASME Turbo Expo 2011: GT2011-45689

In this paper, a prototype fourth generation DLE burner was investigated. Emission, namely NO_X and CO, was monitored for gases with varying fuel compositions. The equivalence ratios of the different burner sections were varied to isolate the individual role of the different burner sections on NO_X formation.

My contribution, besides being the lead author, was choosing the test scheme settings and setting up the emission system. I also did the PSR simulations and the reaction flow analysis. R. Whiddon set up the control system for the atmospheric setup and aided in the analysis of the results. M. Aldén and J. Klingmann supervised the writing.

Error report: Due to a miscalculation of viscosity, the presented mass-flow values for the A2 gas and the dilute A2 gas are 20 % to high. Both equivalence ratios and fuel mass flows should be multiplied by 0.8 to adjust for this error.

Paper VIII:

Experimental Investigation of Lean Stability Limits of a Prototype Syngas Burner for Low Calorific Value Gases

By: **Ivan R. Sigfrid**, Ronald Whiddon, Marcus Aldén, Jens Klingmann

ASME Turbo Expo 2011: GT2011-45694

In this paper, the lean stability limit for a prototype fourth generation DLE burner was investigated. The lean stability equivalence ratio was defined as when the CO emissions pass 200 ppm. The gases examined were methane and syngas. Additionally, the RPL equivalence ratio was varied to investigate this sections influence on the lean blowout. The flame location inside the RPL was monitored by thermocouples on the outside of the RPL body.

My contribution was choosing the test scheme and setting up the emission system. I also did the PSR simulations and laminar flame speed calculations. R. Whiddon set up the control system for the atmospheric setup and aided in the analysis of the results. M. Aldén and J. Klingmann supervised the writing.

Error report: Due to a miscalculation of viscosity, the presented mass-flow values for the A2 gas and the dilute A2 gas are 20 % to high. Both equivalence ratios and fuel mass flows should be multiplied by 0.8 to adjust for this error.

Paper IX:

Experimental Investigation of Laminar Flame Speeds for Medium Calorific Gas with Various amounts of Hydrogen and Carbon Monoxide Content at Gas Turbine Temperatures

By: **Ivan R. Sigfrid**, Ronald Whiddon, Robert Collin, Jens Klingmann

ASME Turbo Expo 2010: GT2010-22275

In this paper, the laminar flame speed was measured using a Bunsen-type burner. The half-angle methodology was used to calculate the laminar flame speed and the result was corrected for flame stretch. Schlieren imaging was used to capture the flame profile. Methane and five generic gases with varying composition were examined with and without preheated air.

My contribution was choosing the test scheme, performing the laminar flame speed calculations, doing the PIV imaging and the stretch correlations. R. Whiddon set up the Schlieren imaging system and the post-processing of the raw images to extract the flame angle. R. Collin and J. Klingmann supervised the writing.

Appendices

APPENDIX A

Flow visualization using Proper Orthogonal Decomposition

Proper orthogonal decomposition (POD), Karhunen-loève transform, hotelling transform, single value decomposition or principal component analysis are all names of the same mathematical procedure. In fluid dynamics, the first name is most commonly used [86-89]. POD uses an orthogonal transform to project the original data set onto a new set that is linearly independent, i.e. orthogonal. The new data set is reduced in size and can be used to reconstruct the original data set. The procedure is strongly related to linear curve fitting in multi-dimensional space [90]. For a two-dimensional problem the data set will be projected onto the direction of largest variance. For a discrete multi-dimensional problem, as for a set of PIV images, the new orthogonal data set, e.g. modes, can be calculated by solving the following eigen value problem (A.1).

$$[K][\varphi] = [\varphi][\lambda] \tag{A.1}$$

The modes (the new orthogonal vector set) $[\varphi]$ can be used to reconstruct the original data set together with their corresponding ensemble coefficient [86]. In papers IV and V [23,43], 4000 PIV images were decomposed. Approximately 500 modes were needed to reconstruct the images without any visible difference between the reconstructed images

and their original. For this highly turbulent case, this means that the data could be reduced by one order of magnitude. After the POD modes have been calculated the modes can be used to visualize flow phenomena more clearly by removing fluctuating motion from the images. In Figure 5.19, the first 200 modes have been used to reconstruct a single-shot PIV image to visualize a pair of counter-rotating vortices.

The modes themselves can be used to compare CFD calculations with measurements [43]. This way of using POD increases the possibilities of comparing measurements with CFD results beyond only mean and fluctuating vector fields, as the modes capture the dynamics of the flow field. Figures A.1 and A.2, show the same mode calculated with PIV and CFD, respectively. The similarity between the CFD and PIV modes can clearly be seen. The main difference is the axial position of the flow structures. This difference is due to the CFD having problems in simulating the correct size of the recirculation zone [43]. Using the POD modes directly for other purposes should be done with caution as they are not existing flow fields but rather vectors in multi-dimensional space. In an example below, additional possibilities for using POD, when the flow is temporally resolved, are shown.

POD Example - The precessing vortex core

For swirling flows, it is common that a precessing vortex core (PVC) will rotate around the centre axis [91]. In this example, a fixed flow field was created by rotating a generic flow field around the centre axis at radius 3 (Figure A.3). The number of images that was needed for the PVC to rotate one revolution around the centre axis was set to 100. After the POD modes were calculated, it can be seen that the "fractional energy" (Figure A.4), i.e. the eigenvalues corresponding to the respective modes divided by the sum of the eigenvalues, contained in the different modes are rapidly depleting and after 10 modes almost no energy is contained in the modes. The modal fractional energy plot (Figure A.4) also shows that the modes come in pairs.

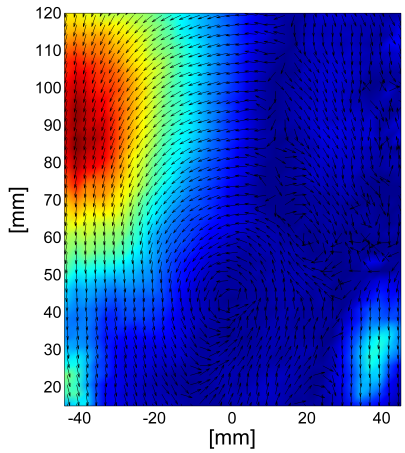

Figure A.1: POD mode from PIV measurements [43]. The vectors are normalized to only show the direction of the flow. The colour bar range is 0 to 1 and shows the absolute value of vectors.

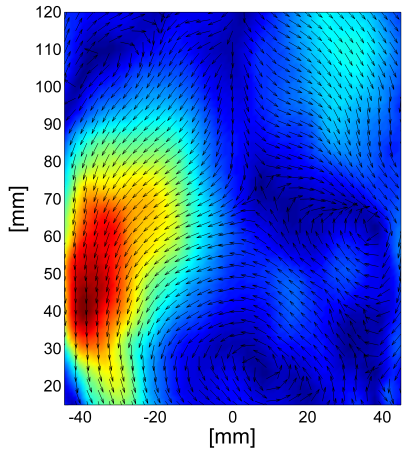

Figure A.2: POD mode from CFD calculations [43]. The vectors are normalized to only show the direction of the flow. The colour bar range is 0 to 1 and shows the absolute value of vectors.

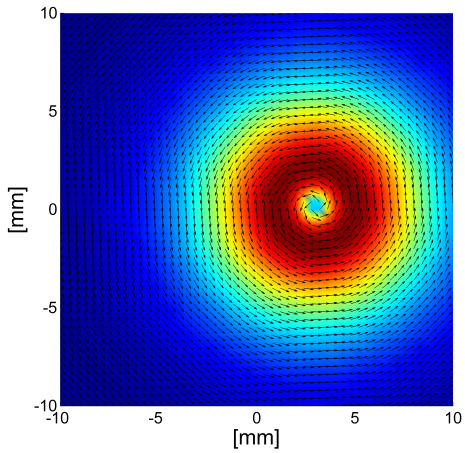

Figure A.3: Illustration of the numerical PVC that is rotated around origo at radius 3. The vectors are normalized to only show the direction of the flow. The colour bar range is 0 to 1 and shows the absolute value of vectors.

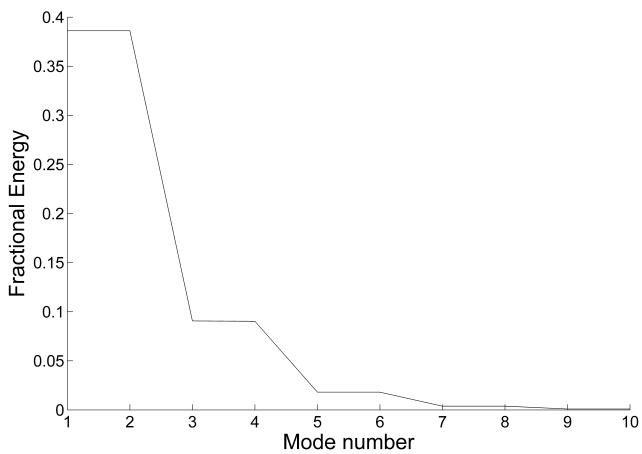

Figure A.4: Fractional energy contained in the first 10 modes.

In fact, the two first modes are representations of the same mode only shifted by 90° (Figures A.5 and A.6). Consequently, in this example, the two first modes form a modal pair. The first modal pair, $m_p = 1$, has two vortices. The amount of vortices in for a modal par can in this example be calculated as (A.2):

$$n_v = 2m_p, \tag{A.2}$$

E.g. modal pair number 2 has 4 vortices and so on (Figure A.7).

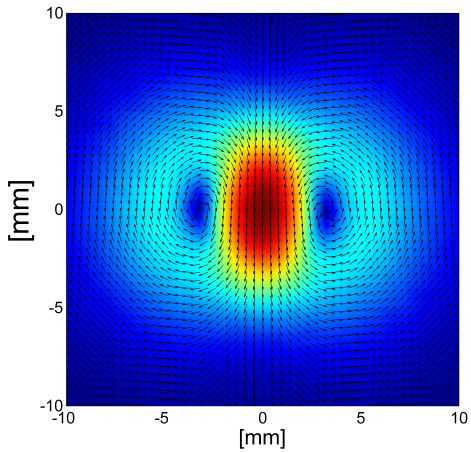

Figure A.5: Mode 1 (modal pair 1)for the PVC. The vectors are normalized to only show the direction of the flow. The colour bar range is 0 to 1 and shows the absolute value of vectors.

The angular shift between the images in the modal pair can also be calculated. For this example the shift in degrees is (A.3):

$$\beta = \frac{90^\circ}{m_p}, \tag{A.3}$$

Plotting the ensemble coefficients for mode 1 (Figure A.8) shows that the frequency is 100, which corresponds to the number of images needed

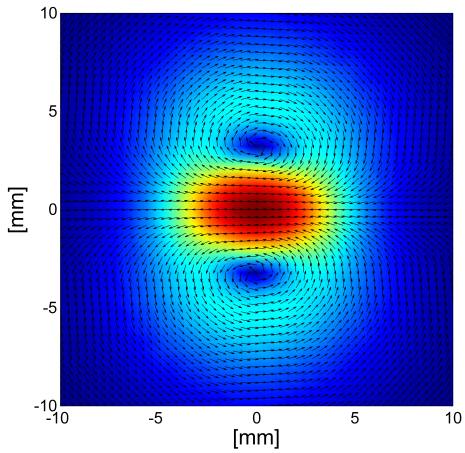

Figure A.6: Mode 2 (modal pair 1)for the PVC. The vectors are normalized to only show the direction of the flow. The colour bar range is 0 to 1 and shows the absolute value of vectors.

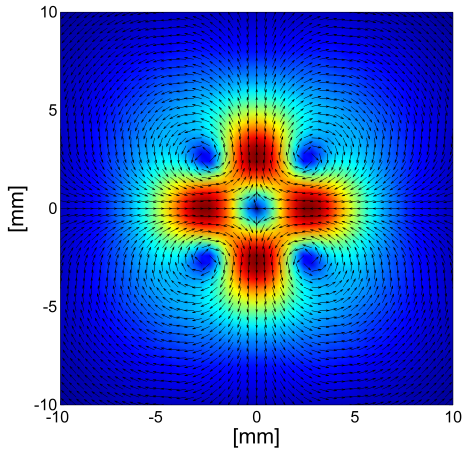

Figure A.7: Mode 3 (modal pair 2) for the PVC. The vectors are normalized to only show the direction of the flow. The colour bar range is 0 to 1 and shows the absolute value of vectors.

for the PVC to take one full turn. The ensemble coefficients quantify how much of each mode that should be used to reconstruct an image. The frequency for specific modal pairs can be calculated as (A.4):

$$f_{m_p} = \frac{f_{m_{p1}}}{m_p}, \tag{A.4}$$

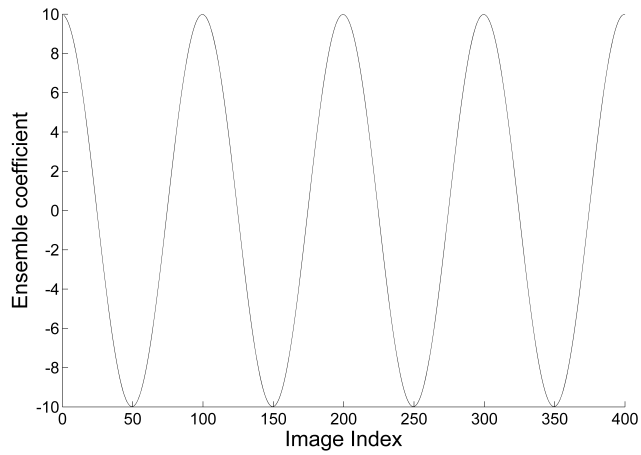

Figure A.8: POD ensemble coefficients plotted against the respective image number.

This example shows that, for time resolved measurements, it should be possible to obtain information about the frequency of specific flow phenomena. It also shows that the individual modes are not an existing flow condition but, as the procedure describes, a decomposition of the flow. Consequently, any analysis directly based on the modes should be carefully performed to avoid ambiguity.

Bibliography

[1] Genrup, M., and Thern, M., 2013, "Ny gasturbinteknik 2012-2014 - Gas Turbine Developments, rapport 2012," Technical Report No. 13:31, Elforsk.

[2] Lieuwen, T. C., and Yang, V., 2005, "Combustion Instabilities in Gas Turbine Engines - Operational Experience, Fundamental Mechanisms, and Modeling," AIAA.

[3] Lieuwen, T., Mcdonell, V., Petersen, E., and Santavicca, D., 2008, "Fuel Flexibility Influences on Premixed Combustor Blowout, Flashback, Autoignition, and Stability," Journal of Engineering for Gas Turbines and Power, 130(1), 011506.

[4] Turns, S. R., 1996, An Introduction to Combustion, McGraw-Hill New York.

[5] Correa, S. M., 1993, "A Review of NOx Formation Under Gas-Turbine Combustion Conditions," Combustion Science and Technology, 87(1-6), pp. 329-362.

[6] Hermann, F., Zeuch, T., and Klingmann, J., 2004, "The Effect of Diluents on the Formation Rate of Nitrogen Oxide in a Premixed

Laminar Flame," ASME Conference Proceedings, 2004(41669), pp. 559-566.

[7] Sigfrid, I. R., Whiddon, R., Abdallah, A.-T., Collin, R., and Klingmann, J., 2013, "Experimental and Reactor Network Study of Nitrogen Dilution Effects on NOx Formation for Natural Gas and Syngas at Elevated Pressures," ASME Conference Proceedings.

[8] Law, C. K., and Sung, C. J., 2000, "Structure, aerodynamics, and geometry of premixed flamelets," Progress in Energy and Combustion Science, 26(4-6), pp. 459-505.

[9] The high-pressure combustion rig
http : //www.forbrf.lth.se/english/research/applications_in_combustion_devices/gas_turbines/the_high_pressure_combustion_rig/

[10] Japikse, D., and Baines, N. C., 1997, Introduction to Turbomachinery / David Japikse, Nicholas C. Baines, White River Junction, Vt. : Concepts ETI ; Oxford : Oxford University Press, 1997.

[11] Moustapha, H., and Zelesky, M., 2003, Axial and Radial Turbines, Concepts NREC.

[12] Walsh, P. P., and Fletcher, P., 2004, Gas Turbine Performance, Blackwell, Oxford, pp. 193-195.

[13] Hada, S., Tsukagoshi, K., Masada, J., and Ito, E., 2012, "Test Results of the World's First 1,600°C J-series Gas Turbine," Technical Report No. Mitsubishi Heavy Industries Technical Review.

[14] Lefebvre, A. H., 1999, Gas Turbine Combustion, Taylor & Francis, New York.

[15] Kurzke, J., 1999, "GasTurb 8.0 - Design and Off-Design Performance of Gas Turbines,"

[16] Longwell, J. P., Frost, E. E., and Weiss, M. A., 1953, "Flame Stability in Bluff Body Recirculation Zones," Industrial & Engineering Chemistry, 45(8), pp. 1629-1633.

[17] Syred, N., and Beér, J. M., 1974, "Combustion in swirling flows: A review," Combustion and Flame, 23(2), pp. 143-201.

[18] Patent Application: 60500518; US class No: 60/747; 60/749; 60/750; International class: F23R 3/12 (20060101).

[19] SIT Gas turbine website: http://www.energy.siemens.com/hq/en/power-generation/gas-turbines/sgt-750.htm

[20] Carrera, A. M., Andersson, M., and Nasvall, H., 2011, "Experimental Investigation of the 4th Generation DLE Burner Concept: Emissions and Fuel Flexibility Performance at Atmospheric Conditions," ASME Conference Proceedings, 2011(54624), pp. 1141-1148.

[21] Sigfrid, I. R., Whiddon, R., Aldén, M., and Klingmann, J., 2011, "Experimental Investigation of Lean Stability Limit of an Prototype Syngas Burner for Low Calorific Value Gases," ASME Conference Proceedings.

[22] Sigfrid, I. R., Whiddon, R., Aldén, M., and Klingmann, J., 2011, "Parametric Study of Emissions from Low Calorific Value Syngas Combustion, with Variation of Fuel Distribution, in a Prototype Three Sector Burner," ASME Conference Proceedings.

[23] Sigfrid, I. R., Whiddon, R., Abou-Taouk, A., Collin, R., and Klingmann, J., 2012, "Experimental Investigations of an Industrial Lean Premixed Gas Turbine Combustor with High Swirling Flow," Proceedings of ASME 2012 Gas Turbine India Conference.

[24] Mathur, M. L., and Maccallum, N. R. L., 1967, "Swirling Air Jets Issuing from Vane Swirlers. Part 1: Free Jets," Journal of the Institute of Fuel, 40(pp. 214 – 225).

[25] Chigier, N. A., and Beér, J. M., 1964, "Velocity and Static-Pressure Distributions in Swirling Air Jets Issuing From Annular and Divergent Nozzles," Journal of Basic Engineering, 86(pp. 788).

[26] Syred, N., Chigier, N. A., and Beér, J. M., 1971, "Flame stabilization in recirculation zones of jets with swirl," Symposium (International) on Combustion, 13(1), pp. 617-624.

[27] Chigier, N. A., and Gilbert, J. L., 1968, "Recirculation eddies in the wake of flameholders," Journal of the Institute of Fuel 41(326), pp. 105.

[28] Smithson, I. K., 1969, "Characteristics of free and confined vortex flow," Ph.D. thesis, Sheffield University,

[29] Lefebvre, A. H., and Halls, G. A., 1959. Some experiences in combustion scaling. Advanced Aero, Engine Testin, Pergamon Press.

[30] Sigfrid, I. R., Whiddon, R., Collin, R., and Klingmann, J., 2010, "Experimental Investigation of Laminar Flame Speeds for Medium Caloricic Gas with Various Amounts of Hydrogen and Carbon Monoxide Content at Gas Turbine Temperatures " ASME Conference Proceedings.

[31] Sigfrid, I. R., Whiddon, R., Collin, R., and Klingmann, J., 2013, "Experimental and Reactor Network Study of Nitrogen Dilution Effects on NOx Formation for Natural Gas and Syngas at Elevated Pressures " ASME Conference Proceedings.

[32] Whiddon, R., Sigfrid, I. R., Collin, R., and Klingmann, J., 2013, "Investigation of a Premixed Gas Turbine Combustor Central Body Burner using OH Planar Laser Induced Fluorescence at Elevated Pressures," ASME Conference Proceedings.

[33] Andrews, G. E., and Bradley, D., 1972, "Determination of burning velocities: A critical review," Combustion and Flame, 18(1), pp. 133-153.

[34] Lantz, A., 2012, Application of laser techniques in combustion environments of relevance for gas turbine studies, Division of Combustion Physics, Department of Physics, Lund University, Lund.

[35] Raffel, M., Willert, C. E., Wereley, S. T., and Kompenhans, J., 2007, Particle Image Velocimetry: A Practical Guide, Springer-Verlag Berlin Heidelberg.

[36] Hulst, H. C., and van de Hulst, H. C., Light scattering: by small particles. Courier Dover Publications, 1957.

[37] Samimy, M., and Lele, S. K., 1991, "Motion of particles with inertia in a compressible free shear layer," Physics of Fluids A: Fluid Dynamics, 3(8), pp. 1915-1923.

[38] Raffel, M., Kompenhans, J., Wereley, S. T., and Willert, C. E., 2007, Particle Image Velocimetry A Practical Guide, Experimental Fluid Mechanics, Springer-Verlag Berlin Heidelberg, Berlin, Heidelberg, pp. 15-18.

[39] Westerweel, J., Dabiri, D., and Gharib, M., 1997, "The effect of a discrete window offset on the accuracy of cross-correlation analysis of digital PIV recordings," Experiments in Fluids, 23(1), pp. 20-28.

[40] Scarano, F., and Riethmuller, M. L., 2000, "Advances in iterative multigrid PIV image processing," Experiments in Fluids, 29(1), pp. S051-S060.

[41] Abou-Taouk, A., Eriksson, L. E., Sigfrid, I. R., and Whiddon, R., 2011, "CFD Investigation of Swirl-Stabilized Flexi-Fuel Burner Using Methane-Air Mixtures for Gas Turbines," International Society for Airbreathing Engines, ISABE.

[42] Abou-Taouk, A., and Lars-Erik, E., 2011, "Optimized Global Mechanisms for CFD Analysis of Swirl-Stabilized Syngas Burner for Gas Turbines," ASME Conference Proceedings.

[43] Abou-Taouk, A., Sigfrid, I. R., Whiddon, R., and Eriksson, L. E., 2012, "A Four-Step Global Reaction Mechanism for CFD Simulations of Flexi-Fuel Burner for Gas Turbines," Turbulence, Heat and Mass Transfer 7, Palermo, Sicily, Italy.

[44] Eckbreth, A. C., 1996, Laser Diagnostics for Combustion Temperature and Species, Combustion Science and Technology book series, 3, Taylor & Francis, London, pp. 84 -86.

[45] Poinsot, T., and Veynante, D., 2011, Theoretical and numerical combustion, T. Poinsot, [S.l.] CNRS.

[46] Warnatz, J., Dibble, R. W., Maas, U., and Springerlink (Online Service), 2006, Combustion Physical and Chemical Fundamentals,

Modeling and Simulation, Experiments, Pollutant Formation, Springer-Verlag Berlin Heidelberg, Berlin, Heidelberg.

[47] Kohse-Höinghaus, K., 1994, "Laser techniques for the quantitative detection of reactive intermediates in combustion systems," Progress in Energy and Combustion Science, 20(3), pp. 203-279.

[48] Puri, R., Moser, M., Santoro, R. J., and Smyth, K. C., 1992, "Laser-induced fluorescence measurements of oh concentrations in the oxidation region of laminar, hydrocarbon diffusion flames," Symposium (International) on Combustion, 24(1), pp. 1015-1022.

[49] Kohse-Höinghaus, K., and Jeffries, J. B., 2002, Applied Combustion Diagnostics, Taylor & Francis Group, New York.

[50] Goldstein, R. J., 1996, Fluid Mechanics Measurements, Taylor & Francis, Berlin.

[51] Lewis, B., and Elbe, G. V., 1987, Combustion, Flames and Explosions of Gases, Academic, Orlando.

[52] Borghi, R., 1985, On the structure and morphology of turbulent premixed flames, Recent advances in the Aerospace Sciences, Springer, London.

[53] Hinze, J. O., 1975, Turbulence, McGraw-Hill Series in Mechanical Engineering, McGraw-Hill, New York.

[54] Pope, S. B., 2000, Turbulent Flows, Cambridge University Press, Cambridge.

[55] Glassman, I., 1996, Combustion, Academic Press New Jersey.

[56] Karlovitz, B., Denniston Jr, D. W., Knapschaefer, D. H., and Wells, F. E., 1953, "Studies on Turbulent Flames: A. Flame Propagation Across Velocity Gradients B. Turbulence Measurement in Flames," Symposium (International) on Combustion, 4(1), pp. 613-620.

[57] Kee, R. J., Coltrin, M. E., and Glarborg, P., 2003, Chemically Reacting Flow : Theory and Practice, Wiley, New York.

[58] DARS – Software for Digital Analysis of Reactive Systems. DigAnaRS, Delaware, USA, *http* : *//www.diganars.com.*

[59] Smith, G. P., Golden, D. M., Frenklach, M., Moriarty, N. W., Eiteneer, B., Goldenberg, M., Bowman, C. T., Hanson, R. K., Song, S., Gardiner Jr, W. C., Lissianski, V. V., and Qui, Z., 1999, GRI-Mech 3.0," *http* : *//www.me.berkeley.edu/gri_mech.*

[60] San Diego Mechanism, 2006 *http* : *//maeweb.ucsd.edu/combustion/cermech/*

[61] Bowman, C. T., 1992, "Control of combustion-generated nitrogen oxide emissions: Technology driven by regulation," Symposium (International) on Combustion, 24(1), pp. 859-878.

[62] Zeldovich, Y. B., 1946, "The oxidation of nitrogen in combustion and explosions," Acta Physicochimica USSR, 21(4), pp. 577-628.

[63] Fenimore, C. P., 1971, "Formation of nitric oxide in premixed hydrocarbon flames," Symposium (International) on Combustion, 13(1), pp. 373-380.

[64] Miller, J. A., and Bowman, C. T., 1989, "Mechanism and modeling of nitrogen chemistry in combustion," Progress in Energy and Combustion Science, 15(4), pp. 287-338.

[65] Myerson, A. L., 1975, "The reduction of nitric oxide in simulated combustion effluents by hydrocarbon-oxygen mixtures," Symposium (International) on Combustion, 15(1), pp. 1085-1092.

[66] Guo, H., Smallwood, G., Liu, F., Ju, Y., and Gulder, O., 2005, "The effect of hydrogen addition on flammability limit and NOx emission in ultra-lean counterflow CH4/air premixed flames," Proceedings of the Combustion Institute, 30(pp. 303-311).

[67] Matuszewski, M., and Jansohn, P., 2012, "Combustion in Gas Turbines with Flue Gas Recirculation," The Future of Gas Turbine Technology 6th International Conference.

[68] Williams, F., 1985, Combustion Theory. Second edition, Addison-Wesley Pub.,Reading, MA, United States.

[69] Law, C. K., 1989, "Dynamics of stretched flames," Symposium (International) on Combustion, 22(1), pp. 1381-1402.

[70] Natarajan, J., Lieuwen, T., and Seitzman, J., 2007, "Laminar flame speeds of H2/CO mixtures: Effect of CO2 dilution, preheat temperature, and pressure," Combustion and Flame, 151(1-2), pp. 104-119.

[71] Hassan, M. I., Aung, K. T., and Faeth, G. M., 1998, "Measured and predicted properties of laminar premixed methane/air flames at various pressures," Combustion and Flame, 115(4), pp. 539-550.

[72] Rozenchan, G., Zhu, D. L., Law, C. K., and Tse, S. D., 2002, "Outward propagation, burning velocities, and chemical effects of methane flames up to 60 ATM," Proceedings of the Combustion Institute, 29(2), pp. 1461-1470.

[73] Vagelopoulos, C. M., and Egolfopoulos, F. N., 1994, "Laminar flame speeds and extinction strain rates of mixtures of carbon monoxide with hydrogen, methane, and air," Symposium (International) on Combustion, 25(1), pp. 1317-1323.

[74] Shanbhogue, S. J., Husain, S., and Lieuwen, T., 2009, "Lean blowoff of bluff body stabilized flames: Scaling and dynamics," Progress in Energy and Combustion Science, 35(1), pp. 98-120.

[75] Yamaguchi, S., Ohiwa, N., and Hasegawa, T., 1985, "Structure and blow-off mechanism of rod-stabilized premixed flame," Combustion and Flame, 62(1), pp. 31-41.

[76] Kundu, K. M., Banerjee, D., and Bhaduri, D., 1977, "Theoretical Analysis on Flame Stabilization by a Bluff-Body," Combustion Science and Technology, 17(3-4), pp. 153-162.

[77] Delattin, F., Lorenzo, G. D., Rizzo, S., Bram, S., and Ruyck, J. D., 2010, "Combustion of syngas in a pressurized microturbine-

like combustor: Experimental results," Applied Energy, 87(4), pp. 1441-1452.

[78] Khalil, A. E. E., and Gupta, A. K., 2013, "Hydrogen addition effects on high intensity distributed combustion," Applied Energy, 104(0), pp. 71-78.

[79] Sayad, P., Schönborn, A., and Klingmann, J., 2013, "Experimental Investigations of the Lean Blowout Limit of Different Syngas Mixtures in an Atmospheric, Premixed, Variable-Swirl Burner," Energy & Fuels, 27(5), pp. 2783-2793.

[80] Schefer, R. W., 2003, "Hydrogen enrichment for improved lean flame stability," International Journal of Hydrogen Energy, 28(10), pp. 1131-1141.

[81] Kumaran, K., and Shet, U. S. P., 2007, "Effect of swirl on lean flame limits of pilot-stabilized open premixed turbulent flames," Combustion and Flame, 151(1–2), pp. 391-395.

[82] Sigfrid, I. R., Whiddon, R., Collin, R., and Klingmann, J., 2013, "Reactive species influence on the lean blow out limit for an industrial DLE gas turbine burner," Combustion and Flame, Submitted.

[83] Driscoll, J. F., 2008, "Turbulent premixed combustion: Flamelet structure and its effect on turbulent burning velocities," Progress in Energy and Combustion Science, 34(1), pp. 91-134.

[84] Lieuwen, T. C., Yang, V., and Yetter, R., 2009, Synthesis gas combustion: fundamentals and applications, CRC Press, LLC.

[85] Tennekes, H., and Lumley, J. L., 1972, A First Course in Turbulence, Cambridge, Mass.

[86] Berkooz, G., Holmes, P., and Lumley, J. L., 1993, "The Proper Orthogonal Decomposition in the Analysis of Turbulent Flows," Annual Review of Fluid Mechanics, 25(1), pp. 539-575.

[87] Chatterjee, A., 2000, "An introduction to the proper orthogonal decomposition," Current Science, 78(7), pp. 808-817.

[88] Holmes, P., Lumley, J. L., and Berkooz, G., 1996, Turbulence, coherent structures, dynamical systems and symmetry, Cambridge monographs on mechanics and applied mathematics, Cambridge Univ. Press, Cambridge, pp. 86 - 128.

[89] Sirovich, L., 1987, "Turbulence and the dynamics of coherent structures. Part 1: coherent structures," Quarterly of Applied Mathematics, 45(3), pp. 561-571.

[90] Pearson, K., 1901, "LIII. On lines and planes of closest fit to systems of points in space," The London, Edinburgh, and Dublin Philosophical Magazine and Journal of Science, 2(11), pp. 559-572.

[91] Syred, N., 2006, "A review of oscillation mechanisms and the role of the precessing vortex core (PVC) in swirl combustion systems," Progress in Energy and Combustion Science, 32(2), pp. 93-161.